Master's thesis

NTNU
Norwegian University of Science and Technology
Faculty of Engineering
Department of Geoscience and Petroleum

Victor de Souza Leao Barros

CFD simulation of the clogging process in a sphere pack

Master's thesis in Petroleum Engineering
Supervisor: Carl Fredrik Berg
Co-supervisor: Hamidreza Erfani Gahrooei
June 2022

NTNU
Norwegian University of
Science and Technology

Victor de Souza Leao Barros

CFD simulation of the clogging process in a sphere pack

Master's thesis in Petroleum Engineering
Supervisor: Carl Fredrik Berg
Co-supervisor: Hamidreza Erfani Gahrooei
June 2022

Norwegian University of Science and Technology
Faculty of Engineering
Department of Geoscience and Petroleum

NTNU
Norwegian University of
Science and Technology

Abstract

During the drilling of an oil well, the phenomenon of drilling fluid escaping from the annular region into the formation is known as lost circulation. Besides the financial and time losses due to mitigation procedures, there is also the possibility of damaging the formation. A potential solution to the lost circulation problem is adding solid particles to the drilling fluid, known as Lost Circulation Materials (LCM). These particles can seal fractures and highly permeable zones. In this work, the rock formation is simplified to a spheres pack. The numerical simulation is performed via the Dense Discrete Phase Model (DDPM), which solves the fluid flow equations and the particle-fluid interactions, coupled to the Discrete Element Method (DEM), which solves the interaction between particles and between particles and walls. Characterization of the liquid-solid flow is obtained by varying the pressure difference in the numerical domain. Fluid velocity, solid particle flow rate, and normalized fluid flow rate are monitored throughout the clogging process. The effectiveness of changing some parameters is studied in this work. Increasing particle diameters shows to be a good solution to reduce fluid loss. The variation in particle-fluid density ratio on the other hand presented little change in the final fluid flow rate. Injecting particles of different sizes can be effective if all particles are larger that the pore throat. The increase in the pressure difference on the domain results in a lower fluid flow rate, but also in fewer particles trapped in the porous medium.

Sammendrag

Fenomenet med borevæske som slipper ut fra brønnen og inn i formasjonen under boring av en oljebrønn er kjent som tapt sirkulasjon (lost circulation). Ved siden av økonomiske tap på grunn av tapt tid ved boring, er det også mulighet for å skade formasjonen. En potensiell løsning for å hindre tap av borevæske er å tilsette partikler til borevæsken, kjent som Lost Circulation Materials (LCM). Disse kan tette brudd og permeable soner. I denne oppgaven er formasjonen forenklet til en kule-pakke. Den numeriske simuleringen utføres med en Dense Discrete Phase Model (DDPM), som løser væskestrøm ligningene og partikkel-væske-interaksjonene, koblet til en Discrete Element Method (DEM), som løser partikkel interaskjoner; kontakter mellom partikler og mellom partikler og pore-vegger. Karakteriseringen av væske-partikkel strømmen oppnås ved å variere trykkforskjellen over modellen. Væskehastighet, partikkelmassestrøm, permeabilitet og volumetrisk strømningshastighet på væsken overvåkes under tilstoppingsprosessen. Økningen i trykkforskjellen på innløpsoverflaten resulterer i en høyere væskehastighet ved innløpsoverflaten og en høyere massehastighet for faste partikler. Det reduserer også den volumetriske strømningshastigheten ved utløpet, noe som resulterer i en mer effektiv tetting av det porøse mediet.

Contents

Figures

Tables

Chapter 1

Introduction

The transport of solid particles by fluid flow is commonly observed in nature and can also be found in many industrial applications, such as water purification (Svarovsky 2001), colloid transport (Bradford and Torkzaban 2008), flows in biological systems (Sanderson *et al.* 2001). In the oil and gas industry, it can be observed in situations like sand production in oil reservoirs (Papamichos *et al.* 2001), gas production from hydrate-bearing sediments (Jung, Jang *et al.* 2012), and in water injection (Hwang and M. M. Sharma 2014). The present chapter introduces the lost circulation problem, the corrective measures to reduce it, and the objectives of the present work. This chapter is based on the author's previous project report.

1.1 Lost circulation

Lost circulation is defined as the loss of the drilling fluids used in the process of well drilling and completion to formation voids (Howard and Scott 1951). A schematic representation of the lost circulation phenomenon in the wellbore is presented in Figure 1.1, based on the work of Howard and Scott (1951). The radius of the drill string is considered as R_c and the radius of the well as R_w. The drilling fluid is injected through the column with a volumetric flow rate Q_{in}. After passing through the drill, it returns to the surface carrying the gravel through the annular region with a volumetric flow rate Q_{out}. The invasion phenomenon occurs through the wall of the well, with a volumetric flow rate Q_{lost}, due to mass balance this can be expressed by the relationship $Q_{in} = Q_{out} + Q_{lost}$.

Lost circulation has proven to be a challenge during the process of construction of wells. Over the years, lost circulation has been responsible for up to 40% the costs of Non-Productive Time (NPT). Krygier *et al.* (2020) defines NPT as the time spent on any unplanned event when operations are stopped or the rate of penetration (ROP) is very low. Lost circulation causes financial loss of approximately 2–4 billion dollars annually, summing lost productive time, lost drilling fluid, and materials used to stem the losses (Cook *et al.* 2011). Aadnoy and Looyeh (2019) estimates that between 10% to 20% of the total time of construction of a well

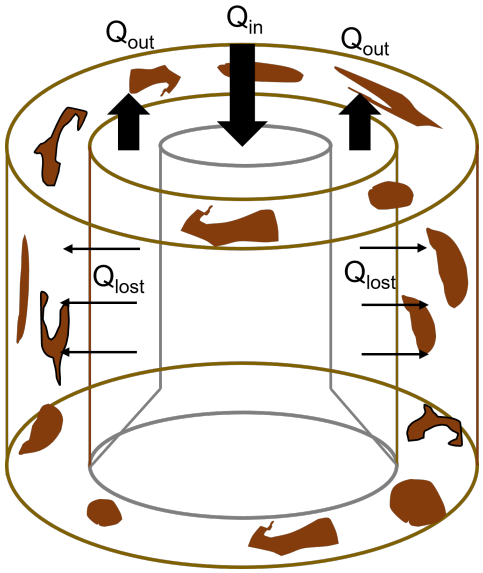

Figure 1.1: Schematic representation of the lost of circulation phenomenon. Adapted from Howard and Scott (1951).

is dedicated to corrective or preventive measures for lost circulation. The invasion of drilling fluids can also cause damage to different types of rock formations (Ezeakacha *et al.* 2018).

During the process of wellbore drilling, drilling fluid is injected through the drilling column to control the pressure in the rock formation (Committee *et al.* 2011). The behavior of the well's pressure as a function of the depth of the well is illustrated in Figure 1.2. If the pressure in the annular region is smaller than the pore pressure, as in the Under-balanced Drilling (UBD) zone, it could lead to the occurrence of kicks, meaning that the formation fluids escape to the wellbore. If the pressure is smaller than the borehole stability pressure, the situation can evolve to a blowout, which is the uncontrolled release of reservoir fluid to the surface, (Caenn *et al.* 2011). The Managed Drilling Pressure (MDP) is the ideal condition of drilling, where the well-bore is stable (Gala and Toralde 2011). However, if the drilling occurs in Overbalanced conditions, there is a possibility of the inflow of the drilling fluid into the permeable rock formation, a phenomenon known as lost circulation (Lavrov 2016). If the pressure inside the annulus is higher than the fracture initiation pressure, it means that permanent damage to the rock formation can occur.

The lost circulation intensifies if the well passes through discontinuities in the geological substrate. The types of formations that are susceptible to loss of circulation are: natural fractures, drill-induced fractures, cavernous formations, and regions with high permeability (Almagro *et al.* 2014). Some examples are illustrated in Figure 1.3.

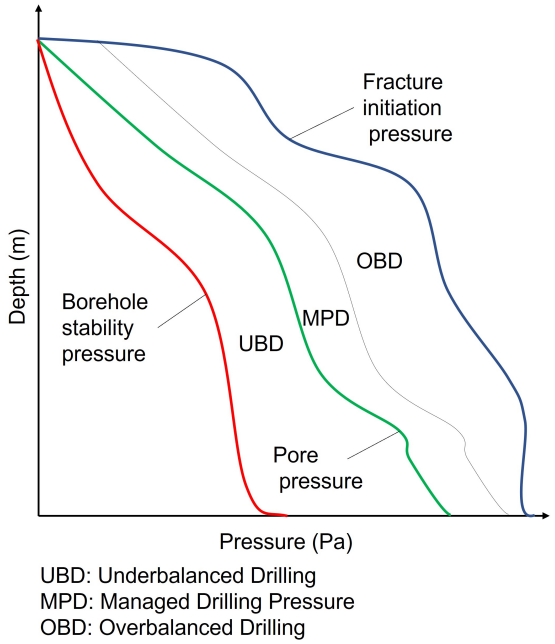

Figure 1.2: Operation window for pressure in an oil well. Adapted from Elliott *et al.* (2011).

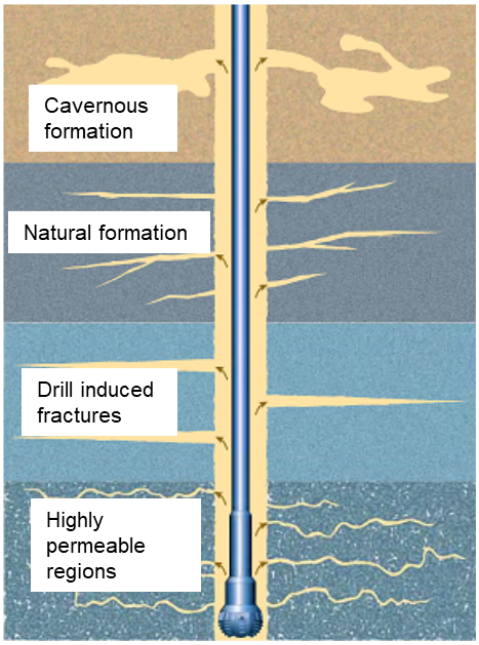

Figure 1.3: Schematic representation of severe regions in the process of lost circulation. Adapted from Almagro *et al.* (2014).

1.1.1 Combative solutions

There are several methods to prevent and combat lost circulation, as studied by Ghalambor *et al.* (2014) and listed in Table 1.1. A method widely used is the addition of solid particles with selected sizes to the drilling fluid, known as Lost Circulation Materials (LCM) (Whitfill and Hemphill 2004). When the fluid is flowing upward in the annulus, the LCM will be sucked by the porous medium due to the pressure difference. It will create a layer of particles that clogs the porous medium, acting as a filter and reducing the flow of drilling fluid.

Table 1.1: Lost circulation solution selection guidelines

Classification	Typical loss rate	Typical formation characteristics	Preventative solutions	mitigation solutions
Seepage	<10 bbl/h	Sand, sand stones, silt	Particulate LCM, manage pressure drilling, drilling with casing	Particulate LCM
Partial	10 to 50 bbl/h	Unconsolidated sand or gravel, small natural fractures, small induced fractures	Particulate LCM, manage pressure drilling, drilling with casing, solid expandable systems	Particulate or fiber LCM, cross-linkable LCM
Severe	>50 bbl/h	Unconsolidated sand or gravel, large natural fractures, large induced fractures	Manage pressure drilling, drilling with casing, solid expandable systems	Particulate or fiber LCM, cross-linkable LCM
Total	no return	Cavernous formations, large and/or numerous natural formations, large and/or numerous induced formations	Manage pressure drilling, drilling with casing, solid expandable systems	Particulate or fiber LCM, cross-linkable LCM

The deposition of solids in the porous medium can occurs in two different ways. Particles smaller than pore throats can travel through the rock formation and sediment inside the pores, clogging the porous media (Rogers 1948). For the particles larger than pore throats, they agglomerate outside the porous media, forming a filter called a mud cake formation (Rabbani and Salehi 2017). The accumulation of particles reduces the invasion of the mud solids and filtrates, as illustrated in Figure 1.4. If an effective mud cake is formed, the mud filtration rate is independent of the overbalance drilling pressure. This phenomenon happens since the mud cake permeability decreases with increasing overbalance pressure. In cases of low permeability formations, a mud cake may not be formed at all due to such small fluid flux that no particle can be deposited on the face of the rock core (Jiao and M. Sharma 1993).

1.2 Objectives

In the present work, we analyze the effectiveness of the injection of solid particles (LCMs) with the drilling fluid to reduce lost circulation. We present a simplified model of a porous medium that can reproduce the same characteristics as the rock formation found in drilling wells. The goal is also to present a mathematical and numerical model for the liquid-solid flow to clog a porous medium using an Euler-Lagrange approach. In this study, the flow will be numerically simulated using the hybrid method of Dense Discrete Phase Model-Discrete Element Method (DDPM-DEM), further discussed in Chapter 4. In the present work, the variables studied are: particle diameter, particle-fluid density ratio, and pressure difference in the

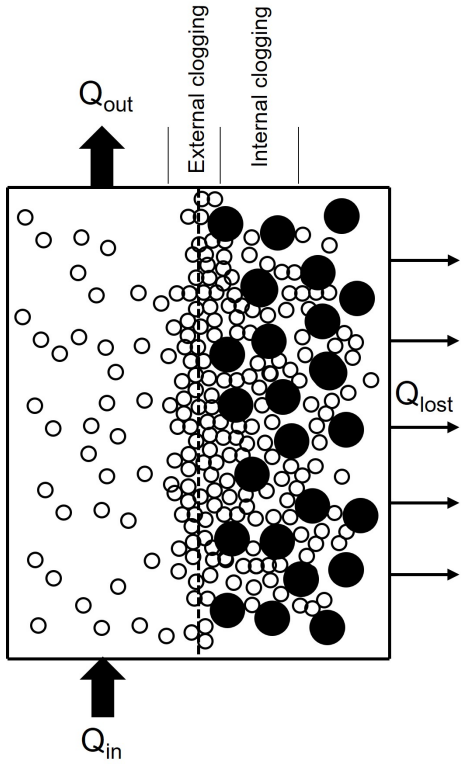

Figure 1.4: Schematic representation of LCMs being used to clog a porous medium.

domain. We also test different combinations of particles in the same simulation. The parameters monitored are the solid particle flow rate, fluid velocity on the outlet surface, the fluid volumetric flow rate at the outlet, and normalized fluid flow rate at the outlet.

Chapter 2

Background

Liquid-solid flow in porous media is a topic that is studied by many researchers, analyzing different numerical methods or presenting experimental apparatus to reproduce the clogging process. In this chapter, a brief list of relevant works for the theme is presented, separated into the numerical approach and the experimental approach. The articles presented in this chapter are based on the author's previous specialization project report background chapter.

2.1 Numerical

When numerically studying liquid-solid flow in porous media, different numerical methods can be adopted, the porous media can be represented in different forms, and different variables can be monitored. The present section presents relevant articles that analyze liquid-solid flow in porous media through a numerical study and the similarities and divergences in comparison with the present thesis.

N. Patankar and Joseph (2001) numerically simulated a liquid-solid flow, where the fluid phase continuity and momentum equations are solved in an Eulerian grid. At the same time, the motion of solid particles is governed by Newton‘s law thus following a Lagrangian approach. The authors considered the drag force from the fluid, body force, and forces due to inter particles stress. The continuity and momentum equations of the fluid, in addition to the position and velocity equations of the particles of the present work, were based on N. Patankar and Joseph (2001) numerical schemes. To validate the numerical scheme, the N. Patankar and Joseph (2001) simulate the sedimentation experiment of Davis *et al.* (1982). The numerical results were in good agreement with the experimental results, validating the calculations by the numerical schemes.

Lima *et al.* (2017) performed numerical simulations of the particle flow through a vertical heterogeneous porous channel using a combination of the Dense Discrete Phase Model (DDPM) together with the Discrete Element Method (DEM). The model solves the equations for the continuum (fluid) and the discrete (particles) phases separately. The present thesis also uses the combined numerical method of DDPM-DEM to reproduce the liquid-solid flow and investigate the influence of

the solid particles and hydrodynamic properties in the clogging process. Unlike the present work, Lima *et al.* (2017) also studies the effects of the porous medium proprieties. Lima *et al.* (2017) analyzed the clogging process on the porous domain by variating the porous domain permeability, the diameter of the particles, the mass flow rate of the particles, and investigates the effects over both the pressure and permeability of the outcome medium. The fluid is considered Newtonian, with constant proprieties, the flow is assumed laminar, and both the fluid and solid are isothermal. It was concluded that the formed mud cake depends mainly on injection time and particle mass flow rate, being higher for larger values of these parameters. A higher particle mass flow rate increases the pressure drop and reduces the time for a stable pressure drop to be achieved.

Kokubun *et al.* (2019) studied the transport of particles in water flow in porous media in order to understand the accumulation of particles and the process of clogging. The present study also studies the clogging process in a porous medium, but Kokubun *et al.* (2019) generates a porous medium in a random way, while the present work considers a regular sphere pack. Kokubun *et al.* (2019) used numerical simulations to evaluate the influence of parameters of interest, such as Stokes number, Reynolds number, and particle-to-water mass densities ratio. The model for pore-scale transport of water and particles is solved in artificially generated two-dimensional porous media. The numerical results show that for homogeneous media, significant accumulation occurs in low-velocity regions. Whereas in heterogeneous media significant accumulation occurs in both low and high-velocity regions. In the high-velocity region, the accumulation of particles leads to the formation of a clog, which causes a redistribution of the pressure on the upstream side and consequently to flow diversion.

Poletto *et al.* (2020) performed a numerical simulation of the injection of LCM in production well to represent the process of mud cake formation to combat the lost circulation problem. The present work also tries to solve the same problem of lost circulation with the injection of LCMs. However, Poletto *et al.* (2020) represents the porous medium as a staggering array of cylinders, while the present thesis represents it as a sphere pack. Poletto *et al.* (2020) simplifies the domain as a vertical channel in contact with a horizontal channel containing a porous medium. The variables analyzed were the Reynolds number in the inlet surface and the initial fluid loss ratio. It was discovered that increasing the Reynolds number in the inlet surface leads to fewer particles being dragged toward the porous domain and eventually a smaller tendency of the particles to sediment. The initial fluid loss ratio is found to be directly related to the number of particles forming the bed.

Parvan *et al.* (2020) investigated the process of clogging by considering the retention of solid particles with different shapes and volumes immersed in the fluid phases on the surface of grains. Parvan *et al.* (2020) also studies the numerical representation of clogging porous media but does it with a different numerical approach. According to Parvan *et al.* (2020), the LBM method is best suited to simulate viscose flow in complex porous media geometries. Parvan *et al.* (2020)

created six different porous media based on X-ray computed tomography, alternating the porosity and topology of the grains. The study uses the lattice-Boltzmann method (LBM) to simulate the fluid flow in porous media and the transport of particles. The porous media with an intermediate size (relative to the range of pore sizes present in porous media) were the most affected by clogging. In the beginning, the main flow streamlines were short and uniformly distributed along with the domain. However, during clogging, streamlines decreased in number and became much longer, which presents an increase of tortuously in the presence of pore-clogging.

Z. Li *et al.* (2021) used a pore network model to study the particle jamming process and compared the results with other numerical methods, such as the CFD-DEM model. The present work reproduces the Z. Li *et al.* (2021) representation of the contact of solid particles numerical as springs and dashpots method. Z. Li *et al.* (2021) extracted all networks from randomly sphere packs, which are constructed using the algorithm developed by Thane (2006). They analyzed the effects of the pore/particle ratio particle concentration and coefficient of friction. It was concluded that the jamming probability decreases linearly with the pore/particle size ratio. It was also concluded that higher particle concentration increases the probability of jamming and that increasing the coefficient of friction also increases the probability of jamming. The numerical method used by Z. Li *et al.* (2021) proved itself to be more applicable in small particle concentration situations.

2.2 Experimental

The study of liquid-solid flow in porous media can also be conducted with experimental apparatus. The present section presents relevant articles about the subject and describes the experimental equipment used and the similarities with the present thesis.

Bacchin *et al.* (2014) studied pore blocking by the use of microfluidic devices. The present work also replicates a porous media as a uniform arrangement in the pore scale, but in a numerical way. Bacchin *et al.* (2014) studies the clogging of porous media on a smaller scale than the present study. Bacchin *et al.* (2014) made microseparators that constituted of an array of microchannels of 20×10^{-6} m wide with three types of structure: straight microchannels, connected microchannels, and staggered square pillars. A constant initial velocity in the larger upstream channel was imposed by a syringe pump feeding the dispersion of solid particles. The microseparators were placed on the stage of a microscope, and images were acquired using a high-sensitivity camera. The results show that for straight parallel channels at high velocity, the clogging is the consequence of arches formation at the channel entrance leading to a cake formation, while for lower fluid velocity, only dendrites (accumulation on pillars) are observed. On staggered square pillars, a progressive plugging of the internal spaces occurs. For connected channels, an intermediate clogging behavior is observed, and the distribution of the flow inside the channels is modified. Then, the dead connection zone between pores

can be swept.

Ahfir *et al.* (2017) investigated the effects of porous media grain size distribution on the transport and deposition of solid suspended particles under different flow velocities. In this present thesis, the velocity of the fluid is also analyzed when studying the influence of the pressure difference in the domain. However, the effects of grain size distributions are not a topic in the present work. Ahfir *et al.* (2017) tested three porous media, two porous media calibrated by their grain size distribution (GSD)(fine sand (315–630 $\times 10^{-6}$ m), and coarse sand (630–800 $\times 10^{-6}$ m)), and a third one which was the result of mixing the first two porous media. The experiments were performed in a horizontal column under constant flow conditions using the step-input injection technique. It was concluded that low flow velocity favors solid particles removal early in the porous medium by straining and gravity, resulting in high non-uniform deposition profiles at the beginning of the porous medium. A high flow velocity carries the particles deeper into the porous medium, producing more gradual changes in the deposition profile with depth.

Wang *et al.* (2016) investigated experimentally the clogging behavior of solid particles in fractured thief zones to combat lost circulation. This work also tries to analyze the impact of the solid particle parameters in the reduction in lost circulation in thief zones. But unlike Wang *et al.* (2016), the present work tries to reproduce high permeable zones, and not induced fractures. Wang *et al.* (2016) analyzed the effect of the parameters of the solid particles, such as particle diameter, material, and concentration on the plugging process. The experimental apparatus consists of a syringe pump for powering the system, a pressurized cylindrical tank, a cylindrical sleeve, and a vessel used for the collection of leakage drilling fluid. The experiment is described as pouring drilling fluid containing the LCM into the tester and applying pressure to determine how well the LCM plugged the slots, then relieving the pressure and finally the artificial fractured core is pulled out to observe the plugging location and tightness of the LCMs in the fracture. The authors concluded that rigid granules work better as bridging material, while powder material is more suitable as filling material. It was also verified that the total fluid loss decreases as the particle concentration increase.

Jung, Cao *et al.* (2018) use microfluid pore models to study the migration of solid particles and the clogging behavior in a structure mimicking porous media. The present thesis also tries to study the effects of particle size in the clogging process in porous media. Unlike the present work, Jung, Cao *et al.* (2018) also investigated the effects of the porous medium pore throat in the clogging results. The experimental apparatus of Jung, Cao *et al.* (2018) consisted of microfluid pore models placed horizontally on a microscope stage connected to a precision syringe pump. The results show that neither clogging nor bridging is observed for higher pore throat to fine particle size ratio, but clogging easily occurred in lower pore throat to fine particle size ratio, even with a low amount of fine particles. It was also determined that the concentration of fine particles required to form clogging or bridging in pores increased as the flow rate decreased.

Zhang *et al.* (2018) studied the internal movement of solid particles in pores and the clogging evolution directly, focusing on the accumulation of the particles. Zhang *et al.* (2018) also represent the porous media as a pack of spheres, like the present work. The porous media created in this work is composed of spheres of the same size, while the one in Zhang *et al.* (2018) experiment is formed of spheres of multiple sizes. The experimental apparatus consisted of a flume, circulating water tank, water pump, constant water supply tank, and HD camera. They studied the effects of the porous porosity, horizontal runoff velocity, initial fluid velocity, and particle size distribution on the clogging development with time, clogging development rate, and particle distribution in the clogging state using the control variable method. Higher porosity leads to the particles in the uppermost layer to gradually decrease and to the deep particles gradually increase. As the horizontal runoff speed increases, the peaked clogging area process is delayed. The time to reach the peak value for the process of clogging with coarse sand is less than that of fine sand.

Chapter 3

Theoretical foundation

The present chapter presents the theoretical foundation of the clogging phenomena in porous media. Relevant concepts are addressed, such as porous media parameters, the scale of representation, liquid-solid flow, and the filtration process. The definitions presented in this chapter are based on the author's previous project report.

3.1 Fluid flow in porous media

A porous medium is characterized as a material consisting of a solid matrix with an interconnected void space. The solid matrix has to be either rigid or is allowed to undergo small deformation. The interconnections of the void must allow the flow of one or more fluids through the material (Nield, Bejan *et al.* 2006), in the present work only one fluid is used. In permeable media, the pores form a continuous network of channels of different sizes that offer resistance to flow (Dullien 1991).

3.1.1 Pore structure parameters

Pore structure parameters are those properties that are determined by the pore structure of the medium (Dullien 1991). The properties important to the present study are porosity (ϕ) and permeability (K).

Porosity

The definition of porosity, ϕ [-], is the fraction of the bulk volume of the porous sample that is occupied by pore space (Dullien 1991). There can be two kinds of pore spaces: interconnected, which forms a continuous phase of the pore medium; and isolated, in which the pores are disconnected. Total porosity can be quantified as in Equation (3.1), assuming V_s [m^3] is the volume of solid and V_b [m^3] is the volume of the bulk.

$$\phi = 1 - \frac{V_s}{V_b} \tag{3.1}$$

In the present work, it is considered a connected porosity, which is defined as the void space where an uninterrupted path exists between the borders of a volume (Géraud *et al.* 1992). Since the object of study of the present work is high permeable rock formations, we consider the porosity as macroporosity () $> 10^{-6}$) m (Thomas *et al.* 2019).

Permeability

The permeability, K [m^2/s], can be described as the property of a system to be able to be passed through by a fluid (Dullien 1991). It can be represented by Darcy's law in the differential form, Equation (3.2).

$$v = -\left(\frac{K}{\mu}\right)\nabla\varrho = -\left(\frac{K}{\mu}\right)(\nabla P - \rho g z) \tag{3.2}$$

Equation (3.2) is dependent not only of K [m^2], but also v [m/s], the fluid velocity; z [m], the distance measured vertically upward; μ [cp] the fluid viscosity; P [Pa], the hydrostatic pressure; and g [m^2/s], the acceleration due gravity. It is assumed that ϱ is equal to $P + \rho g z$, and it is measured by an apparatus call piazometer. This special equipment was used in the studies of Bear (1988), as presented in Figure 3.1.

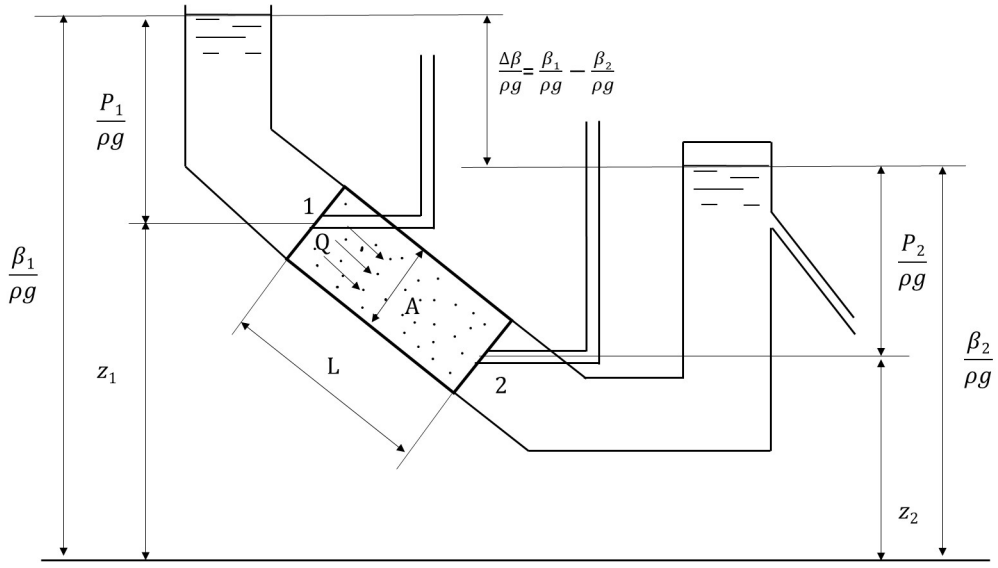

Figure 3.1: Illustration of a piazometer, adapted form Bear (1988).

In the present work, the height will not be relevant for the permeability calculation, so z=0. It is assumed that v=$Q_{f,o}/A$, where $Q_{f,o}$ [m^3/s] is the fluid

volumetric flow rate and A [m^2] is the area perpendicular to the flow. Darcy's law is then integrated in the length direction, so it can be written as Equation (3.3). The permeability unit is represented as the same as the unit for the area, [m^2] since the pore size is the variable that determines the permeability of a medium.

$$K = \frac{Q_{f,o}\mu L}{A\Delta P} \tag{3.3}$$

3.1.2 Porous media classification

Due to the wide variety of shapes and forms of pores, there are several variables that classify porous media:

- pore size;
- type of pores;
- pore shape;
- pore layout.

Cheremskoj (1985) suggested one classification by pore size: sub-micro-scale; micro-scale; macro-scale. Sub-micro pores have a diameter of less than 2×10^{-7} m. Pores in the micro scale have a diameter between 2×10^{-7} m and 2×10^{-6} m. The macro scale pores have a diameter larger than 2×10^{-6} m.

The porous medium can also be classified in relation to the types of pores (Zdravkov *et al.* 2007): interconnected and disconnected pores. Interconnected pores have at least one connection to the rest of the pore network. While the disconnected pores are completely isolated from the other pores

Another method of classifying porous media is in relation to the shape (Maryasev *et al.* 2011): round; extended; twisted. Granules are usually modeled as a set of particles or grains (usually spherical), whereas fibrous ones are modeled as a set of very long inclusions, called fibers. Round shapes are spherical and most common for isolated pores. Extended pores have an elongated rectilinear directed shape, forming a channel. Twisted pores are curved and present an arc-shaped.

Maryasev *et al.* (2011) also classifies porous media according to the spatial arrangement of the pores: random and uniform. A random arrangement of pores is more common in most real-life examples of porous media. But uniform structures are simpler to reproduce and simulate.

The present work represents a macro scale porous media, with interconnected pores, extended channels, and with a uniform arrangement.

3.1.3 Porous media representation

When considering a numerical approach to modeling a porous medium, the size of the pore or fracture of the porous domain must be taken into consideration. A porous medium can be represented in three different scales:

- pore-scale;
- transition scale;

- continuous scale;

In the pore scale, it is possible to differentiate the interface between the fluid phase and the solid phase (Netinger 1994). When the porous medium is treated at the pore scale, therefore the classical Navier-Stokes equation can be used to solve the problem.

The porous medium can also be considered at a transition scale, normally used for problem analysis for the flow of fluid occurring next to a porous medium (Chandesris and Jamet 2009). The fluid and porous media are considered homogeneous and in the interfacial region, there is a transition zone through which the properties of the medium vary continuously (from a porous medium to a void space).

While on a continuous scale, it is not possible to visually distinguish the constituents and the nuance of the pore, so the transport properties are calculated based on effective parameters (Dash *et al.* 1996). An interface between this continuous scale porous medium and a free fluid region is created, and the analysis occurs on a Darcy scale. At the free fluid region, the Navier-Stokes equation can be used, but at the homogeneous porous medium region, the generalized momentum equation for the porous medium is used to model the flow, leading to a two momentum equation for the problem.

All scales are represented in Figure 3.2. The present study analyses the interaction of solid particles and the fluid flow with the porous medium to study the clogging process, therefore we will consider the porous medium at the pore scale.

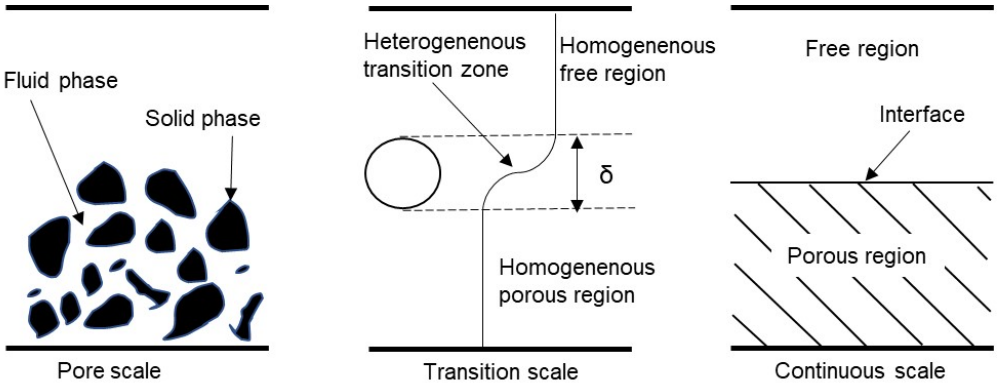

Figure 3.2: Analysis scales for a partially porous medium. Adapted from Chandesris and Jamet (2009).

3.2 Liquid-solid flow

Liquid-solid flow is a type of flow where a discrete phase, the solid, is carried by the continuous phase, the fluid (Crowe 2005). One of the main parameters of classifying a liquid-solid flow is the volumetric fraction of the solid phase in

relation to the continuous phase. The solid volume fraction must be written in an Eulerian perspective, occupying the volume in the domain not occupied by the continuous phase, Equation (3.4).

$$\varepsilon_p = 1 - \varepsilon_f \tag{3.4}$$

The liquid-solid can be classified as dispersed flows or dense flows. Dispersed flows are characterized by the low concentration of solid material so that the particles are far enough apart from each other to disregard any interactions between them ($\varepsilon < 0.1$). Dense flow is characterized by the concentration of particles being so high that the collisions have relevant importance ($\varepsilon > 0.1$)(Peker and Helvaci 2011).

3.2.1 Categorization of liquid-solid flow

Loth (2010) categorized the disperse liquid-solid flow into four categories by referring to the coupling regimes which take place as the solid particles' concentration increases, these are:

- one-way coupling regime: in which the fluid affects the motion of the particles but not vice-versa;
- two-way coupling regime: in which the particles affect the flow field of the carrier fluid;
- three-way coupling regime: in which flow disturbances produced by the particles affect the motion of the nearby ones;
- four-way coupling regime: in which direct particle-particle interactions take place.

When the solid volume fraction is higher than 0.1, the four-ways couplig is assumed to be a dense flow and can be divided into two categories (Loth 2010):

- collision dominated: in which the particle-particle interactions occur in the form of quick inter-particle collisions.
- contact dominated: in which the particle-particle interactions occur in the form of enduring inter-granular contacts.

The categorization of the both disperse and dense liquid-solid flow is illustrated in Figure 3.3, adapted from Messa *et al.* (2021). In this work, it is assumed a four ways coupling contact dominated , since both fluid and particles can affect each other behavior and it occurs particle collision in the simulation. Since there is expected a particle filter formation, the problem can be considered contact dominated.

3.2.2 Numerical solutions of liquid-solid flow

The problem of particles injected in a flow can be numerically solved by different numerical models, as presented in Figure 3.4. The difference between the mod-

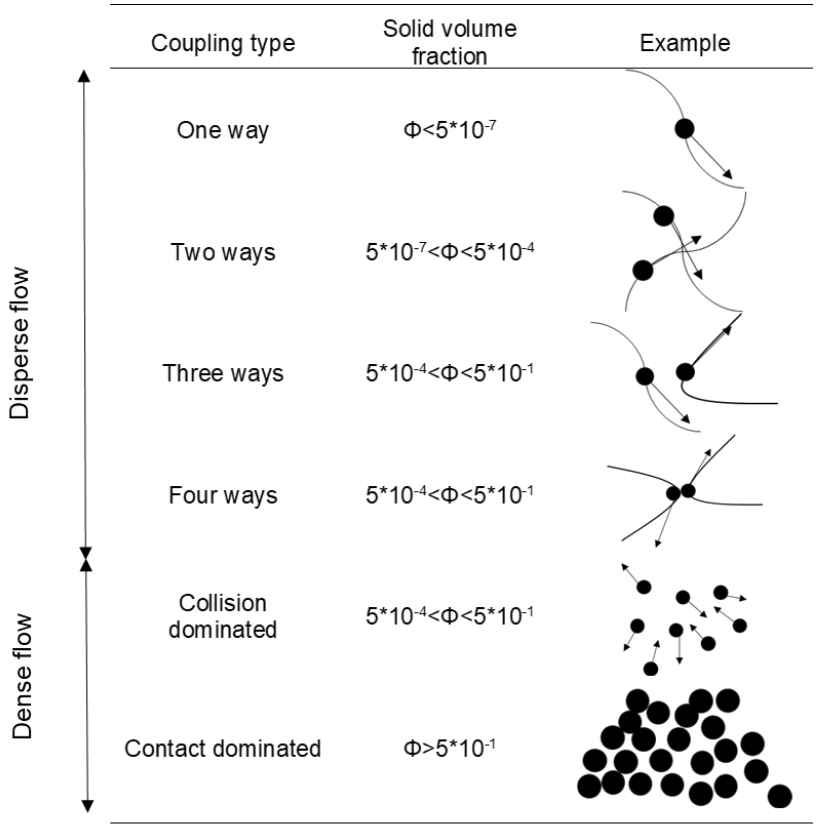

Figure 3.3: Representation of the different types of interaction between particles and the fluid. Adapted from Messa *et al.* (2021).

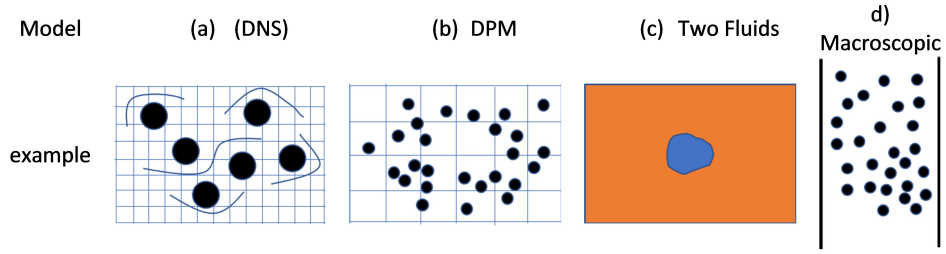

Figure 3.4: Scales of analysis for the liquid-solid flow.

els rely on the individual identification of each particle though the fluid-particle interface.

Figure 3.4 (a) presents the Direct Numerical Simulation (DNS), which takes into account the forces and effects on each particle (Uhlmann 2006). It is possible to observe the kinetic boundary layer, and the formation of vortices at the particles surface. A sufficient amount of mesh nodes on the surface of each particle is necessary to apply this method, so the velocity and pressure fields are correctly calculated. Since it makes such complex calculations, the DNS requires a high number of interactions.

Figure 3.4 (b) illustrates the Discrete Phase Model (DPM), where the effects of fluid on particles, and vice versa, are evaluated using terms that account for mass transfer and momentum (Chiesa *et al.* 2005). In the DPM method the solid particles are smaller than the control volumes, therefore is not possible to calculate the boundary layer formation. The numerical simulation is performed using a Euler-Lagrange approach taking in consideration the effects of one ant two-ways coupling. The four-ways coupling effects can be calculated using the Discrete Element Method (DEM), discussed in 4.3.2, coupled with th DPM method.

Figure 3.4 (c) shows the Two-Fluid Model (TFM), in which the fluid and solid phases are considered as two overlapping continuous phases. This method uses an Eulerian-Eulerian numerical model. The effectiveness of the TFM method relies on the constitutive or closure relations for the solid phase and the momentum exchange between phases (A. B. Yu and B. H. Xu 2003).

Figure 3.4 (d) illustrates the Macroscopic model, where fluid and solid particles are considered as one single continuous medium in which it is impossible to distinguish the dispersed from the continuous phase (Sun and Munn 2005). Specific data of one of the phases are not available in this method, since all parameters are calculated as an average between the two phases.

In the present work it is required to identify the position of each individual particle and a method that do not demand a high number of interactions. Therefore, we decided to use the DPM method since it favors the simulation of a significant amount of particles while still possible to observe the movement of each individual particle.

3.3 Liquid-solid flow in porous media

The filtration process consists of the separation of a mixture of solids and fluids into separate phases and is characterized by three types of processes: remove solid from fluid, remove fluid from solid, and recover both phases (Sparks and Chase 2016). For the process of removing solid from fluid, one of the methods commonly used is deep bed filtration. The method consists in passing the mixture of fluid and solid through a separator agent with obstacles, and the solid particles will deposit through the entire dept of the medium (Mays and Hunt 2005), as demonstrated in Figure 3.5.

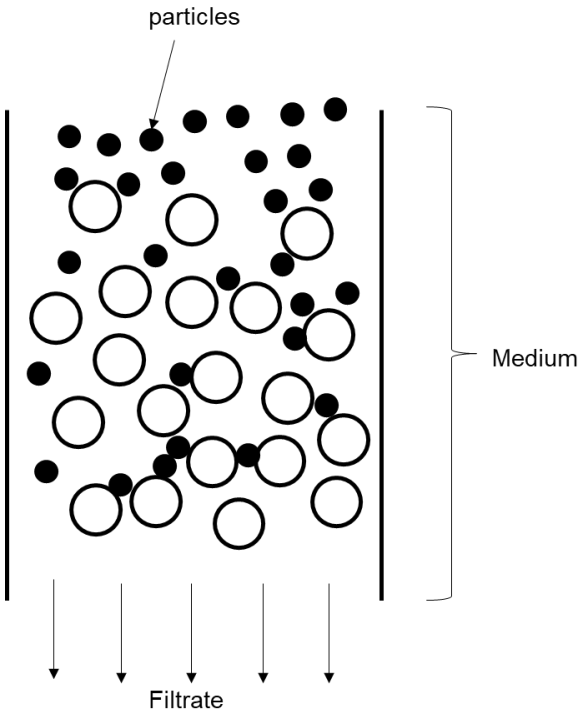

Figure 3.5: Deep bed filtration method. Adapted from Mays and Hunt (2005).

The work of Santos and Bedrikovetsky (2006), presents a literature review of liquid-solid flow in porous media and discusses the size exclusion mechanism. Iwasaki *et al.* (1937) was the first author to introduce a phenomenological model for the particle-capture and permeability damage process. Herzig *et al.* (1970) used such a model to describe the filtration process. The author defined two types of deep filtration formation: mechanical (diameter $> 3\times10^{-5}$ m) and chemical (3.3×10^{-4} m $<$ diameter $< 3.03\times10^{-3}$ m). Shutong and M. M. Sharma (1997) used the model to investigate the injectability decline for water-injection wells. The results were compatible with experimental results, being able to be used for prediction purposes, but not diagnostic purposes.

During the wellbore drilling, the process of particle capture in porous me-

dia can be caused by different physical mechanisms (Elimelech *et al.* 2013). The mechanisms are: size exclusion; electrical forces (Van der Waals, etc.); gravity segregation; and multi-particle bridging. The present work will focus on the size exclusion mechanism, in which large particles are captured in small pores and pass through large pores.

According to Civan (2007), during the sedimentation process, the solid particle can pass through the pore throat and occasionally settle at the base of the porous medium by gravity. An interesting phenomenon that also can occur is the obstruction of the pore throat, which happens when the particle encounters an insurmountable pore throat, creating a seal and hindering the passage of other particles, then formatting a particle bed.

The presence of particles in a porous medium can reduce permeability through two distinct mechanisms, as claimed by M. Sharma and Yortsos (1987): particles larger in size than the pore size are trapped by the pore throat; particles of size significantly smaller than the pore size deposit uniformly over pore throats. In either case, a complete reduction of permeability is reached when a sufficient number of pore throats are blocked, and the conductivity of the medium is zero.

Chapter 4

Methodology

The following chapter presents the modeling of the geometry and the description of its boundary conditions used in our simulations. Then, the equations needed to be solved for the liquid-solid flow are presented. Lastly, the numerical methods used to solve the equations of the flow are described. The simulation methodology presented in this work was developed based on a previous project report methodology chapter by the authors.

4.1 Geometry of the problem

Porous media present in rock formations found in oil wells have complex and irregular geometries (Nield, Bejan *et al.* 2006). Therefore simplifications are common when modeling the porous medium. One way is to approximate a porous medium to a periodic known geometric whose permeability can be validated with an analytical model. Eidsath *et al.* (1983), Coulaud *et al.* (1988) and Sahraoui and Kaviany (1992) considered the domain of interest as a periodic two-dimensional periodic array of cylinders. Lee and Yang (1997) simulated the fluid flow through a bank of cylinders, Larson and Higdon (1989) studied the Stokes flow around a pack of spheres and Inoue and Nakayama (1998) simplified the porous medium as an array of cubes.

For this work, the porous medium is represented as a sphere packing with the face center cubic (fcc) lattice arrangement (Szpiro 2003). The porous medium is arranged in three layers of spheres with 1×10^{-2} m diameter, as illustrated in Figure 4.1. The final porous medium is shown in Figure 4.2. Then, the pack of spheres is embedded in a square channel with dimension of (3.2; 3.2; 5×10^{-2} m), as shown in Figure 4.3. The surface A_s is is equivalent to 1.024×10^{-3} m^2 and the length of the porous medium L is 3×10^{-2} m. To calculate the porosity ϕ, we find the bulk volume V_b as 3.072×10^{-5} m^3 and the volume of solid as 1.41×10^{-5} m^3 (considering 27 spheres of 1×10^{-2} m of diameter). Resulting in a porosity ϕ equal to 0.539.

An initial pressure at the outlet $P_o = 0$ and a predefined initial pressure in the inlet P_i are set as boundary conditions, generating a pressure difference ΔP. The

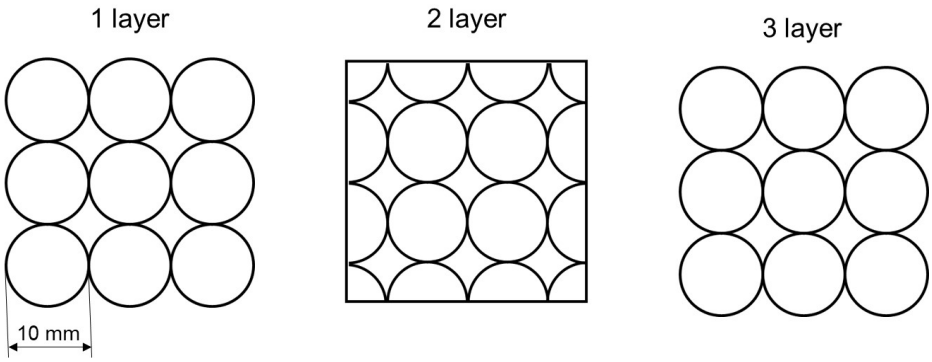

Figure 4.1: Presentation of the three layers of spheres.

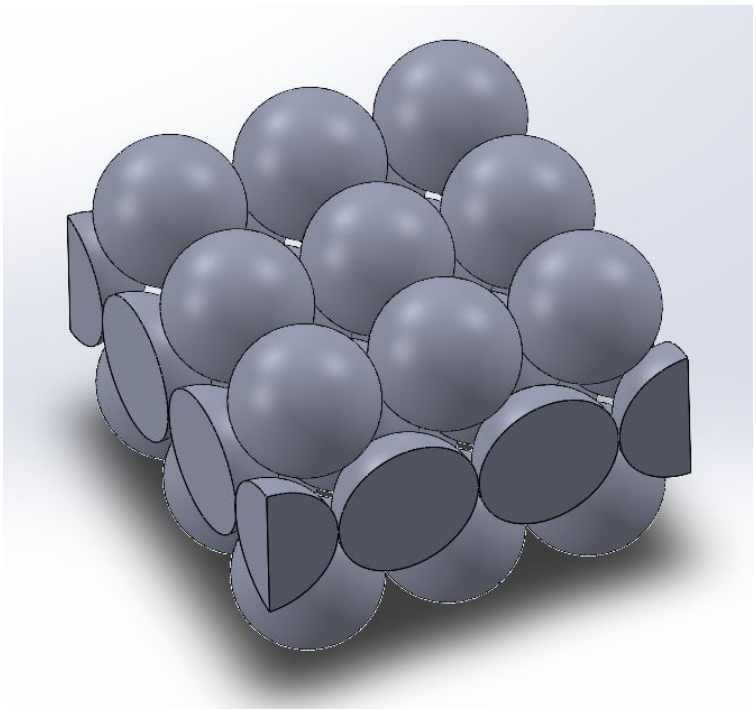

Figure 4.2: Final representation of the pack of spheres.

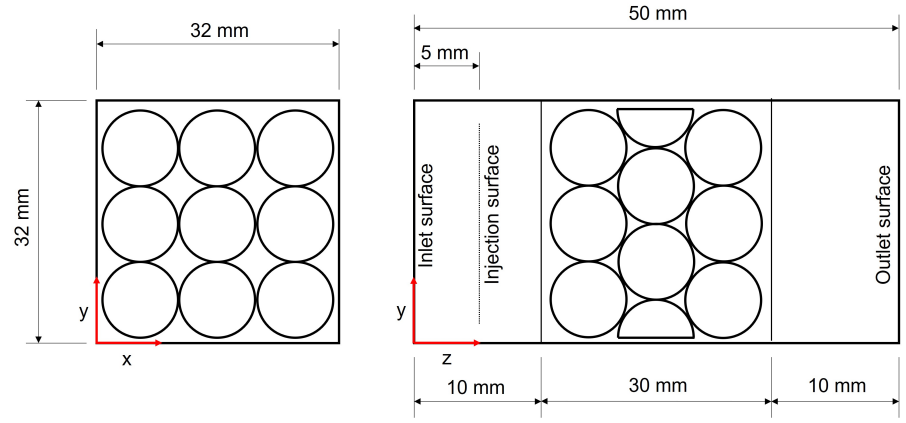

Figure 4.3: Outline of the simulation model.

other surfaces of the channel, as well as the faces of the sphere, are considered no-flow boundaries, with the fluid velocity in the contact being zero. The injection of the solid particles into the domain is done on the injection surface, further explanations in Section 4.4.

4.2 Equilibrium equations

In this work, the liquid flow with the addition of solid particles is considered on the pore scale, making it possible to describe each solid particle individually. The liquid flow is considered the continuous phase and the solid particles injected into the domain are considered the disperse phase, therefore, the mathematical formulation is carried out under a hybrid approach of Euler-Lagrange. The velocity and pressure fields of the continuous phase can be calculated from a set of equations, which must be properly coupled to account for the interaction effects between the fluid and disperse solids. For the fluid flow, the calculations are based on local volume averages. It is solved based on the equations of mass balance and momentum. The equations for the particles' movement are described using Newton's second law.

4.2.1 Continuous phase

For the single-phase fluid flow, the equations for conservation of mass and momentum can be described by the Navier-Stokes equations, Equation (4.1), and Equation (4.2). Assuming that ρ_f [kg/m^3] represents specific mass of the fluid, μ_f [Pa·s] the viscosity, P_f the fluid pressure, u_f [m/s] the fluid velocity and g [m/s^2] the gravity acceleration.

$$\frac{d\rho_f}{dt} + \nabla \cdot \rho_f u_f = 0 \tag{4.1}$$

$$\rho_f \frac{du_f}{dt} = -\nabla P_f + \nabla \cdot (\mu_f \nabla \cdot u_f) g \tag{4.2}$$

The flow is assumed to be laminar, without the occurrence of chemical reactions, with an incompressible and isothermal fluid. The flow is considered three-dimensional, in a cartesian system. The detailed description of the flow in each direction is derived in Appendix A.

For the liquid-solid two-phase flow, the effects of the discrete phase (solid particles) in the continuous phase (fluid) are accounted by the coupling term $f_{p,f}$ [kg/s], which represents the amount of transfer bilateral movement between fluid flow and particles. Since there are two phases accounted for in the simulation, the continuous phase balance equations occur by the inclusion of the volumetric fraction of the solid phase, ε_p, and fluid phase ε_f=1-ε_p. according to Popoff and Braun (2007), a flow is considered dense when ε_p>0.1. Equation (4.3) and Equation (4.4) are defined taking in consideration that for the particulate flow we have ε_f<1 and $f_f \neq 0$. The term $s_{p,f}$ [kg/s] is a source term to compute the exchange of masses between phases. The terms $f_{p,f}$ and $s_{p,f}$ will be further discussed in Section 4.3.2 when describing the DEM method.

$$\frac{\partial(\rho_f \varepsilon_f)}{\partial t} + \nabla \cdot (\rho_f \varepsilon_f u_f) = 0 \tag{4.3}$$

$$\frac{\partial(\rho_f \varepsilon_f u_f)}{\partial t} + \nabla \cdot (\rho_f \varepsilon_f u_f u_f) = \\ -\varepsilon_f \nabla P_f + \nabla \cdot (\mu_f \varepsilon_f \nabla \cdot u_f) + \rho_f \varepsilon_f g + f_{p,f} + s_{p,f} \tag{4.4}$$

4.2.2 Discrete phase

For the present work the particles are considered as spherical, rigid, non-coalescent and indeformable. The properties of the discrete phase (e.g. specific mass of particle, diameter) are uniform. The equations for particle movement are described by Newton's Second Law for translational motion, Equation (4.5) and rotational movement, Equation (4.6). Each individual particle present in the computational domain is denoted by sub index j. The forces F and torques T considered in Equation (4.5) are classified by their sub-index "s", "b" and "c", that means surface, body and collision, respectively. All the forces and torques mentioned are summarized in Table 4.1 and defined in Appendix B. The momentum of inertia of particle j is denoted by $I_{p[j]}$ [kg·m^2]. The expressions for particle velocity u_p [m/s], particle rotation w_p [1/s] and particle position x_p [m] are presented as Equation (4.7), Equation (4.8) and Equation (4.9).

$$m_{p[j]}a_{p[j]} = m_{p[j]}\frac{du_{p[j]}}{dt} = m_{p[j]}\frac{d^2x_{p[j]}}{dt^2} = F_{d,s[j]} + F_{pg,s[j]} + F_{vm,s[j]} + F_{sl,s[j]} + F_{ml,s[j]} + F_{b,s[j]} + F_{g,b[j]} + F_{p,c[j]} \quad (4.5)$$

$$I_p\frac{w_p}{dt} = T_{d,s[j]} + T_{c,s[j]} \quad (4.6)$$

Table 4.1: Summary of forces and torques acting in particle j.

Force	Expression	Equation
Drag force	$F_{d,s[j]} = \frac{1}{2}C_d\rho_f A_{p[j]}\lvert u_{f[j]} - u_{p[j]}\rvert(u_{f[j]} - u_{p[j]})$	Equation (B.1)
Pressure gradient force	$F_{pg,s[j]} = -V_{p[j]}\nabla P_f = m_{p[j]}\frac{\rho_f}{\rho_{p[j]}}(u_{f[j]}\nabla\cdot u_{f[j]})$	Equation (B.2)
Virtual mass force	$F_{vm,s[j]} = C_{vm}m_{p[j]}\frac{\rho_f}{\rho_{p[j]}}\frac{D}{Dt}(u_f - u_p)$	Equation (B.3)
Saffman's lift force	$F_{sl,s[j]} = m_{p[j]}\frac{\rho_f}{\rho_{p[j]}}(w_{f[j]}x(u_{f[j]} - u_{p[j]})C_s l)$	Equation (B.4)
Magnus's lift force	$F_{ml,s[j]} = m_{p[j]}\frac{\rho_f}{\rho_{p[j]}}x(w_{p[j]}x(u_{f[j]} - u_{p[j]})C_{ml[j]})$	Equation (B.6)
Gravity force	$F_{g,s[j]} = \rho_p V_p g$	Equation (B.10)
Buoyancy force	$F_{b,b[j]} = \rho_f V_p g$	Equation (B.9)
Collision force	$F_{p,c[1]} = F_{n[1]}n_{12} + F_{t[1]}t_{12}$	Equation (4.10)
Torque	Expression	Equation
Drag torque	$T_{d,s[j]} = C_{w[j]}\omega_{f,p[j]}$	Equation (4.13)
Collision torque	$T_{n[i]} = \frac{d_{p[i]}}{2}n_{[ij]} * F_{f[i]}$	Equation (4.38)

$$u_p = u_{p,x}e_i + u_{p,y}e_j + u_{p,z}e_k \quad (4.7)$$

$$w_p = \nabla \times u_p \quad (4.8)$$

$$x_p = x_{p,x}e_i + x_{p,y}e_j + x_{p,z}e_k \quad (4.9)$$

The collision Forces $F_{p,c[j]}$ is due to the contact interaction of particle-particle or particle-surface. For the present work it is used a soft sphere approach. Following Hoomans (2000), the collision force can be decomposed in two components, normal force $F_{n,c}$ and tangential force $F_{t,c}$, on the normal vector $n_{[12]}$ and the tangential vector $t_{[12]}$, as presented in Equation (4.10). By Newtons third law, the same normal and tangential forces are also applied to the colliding particle , Figure 4.4.

$$F_{p,c[1]} = F_{n[1]}n_{12} + F_{t[1]}t_{12} \quad (4.10)$$

The velocity of the particles $v_{p[j]}$ can be determined by integrating the acceleration of the particles $a_{p[j]}$, known from Equation (4.5), resulting in Equation (4.11). To determinate the position of the particle $x_{p[j]}$, Equation (4.11) is integrated, which creates Equation (4.12).

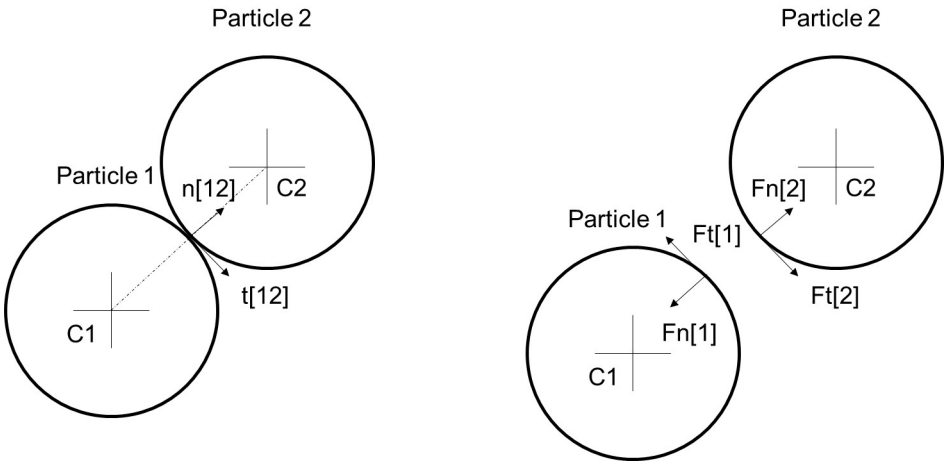

Figure 4.4: Representation of the forces involved on the collision of two particles.

$$u_{p[j]} = \int_{t_{initial}}^{t_{final}} a_{p[j]}\, dt \rightarrow u_{p[j]} = u_{p,x[j]}e_x + u_{p,y[j]}e_y + u_{p,z[j]}e_z \tag{4.11}$$

$$x_{p[j]} = \int_{t_{initial}}^{t_{final}} u_{p[j]}\, dt \rightarrow x_{p[j]} = x_{p,x[j]}e_x + x_{p,y[j]}e_y + x_{p,z[j]}e_z \tag{4.12}$$

Equation (4.6) presents the rotational momentum evaluated by a torque balance, taking in consideration the viscous drag torque $T_{d,s[j]}\,[N{\cdot}m]$, Equation (4.13). The torqueaccelerates the particle due to the existence of relative velocity with the fluid. It is expressed by a function of relative rotation velocity of the particle in relation to the fluid velocity gradient, as given by $\omega_{f,p[j]}$, Equation (4.14), and the rotational friction coefficient $C_{w[j]}$ (Happel and Brenner 2012). The contact torque $T_{c,s[j]}\,[N \cdot m]$ is calculated by the Discreet Elements Method. The moment of inertia of particle j is denoted by $I_{p[j]}\,[\mathrm{kg{\cdot}m^2}]$, Equation (4.15), and the angular velocity by $w_p\,[1/s]$, Equation (4.16).

$$T_{d,s[j]} = C_{w[j]}\omega_{f,p[j]} \tag{4.13}$$

$$\omega_{f,p[j]} = \frac{1}{2}\nabla u_{f,[j]} - w_{p[j]} \tag{4.14}$$

$$I_{p[j]} = \frac{\pi}{60}\rho_p d_{p[j]}^5 \tag{4.15}$$

$$w_{p[j]} = \nabla x u_{p[j]}\, dt \rightarrow w_{p[j]} = w_{p,x[j]}e_x + w_{p,y[j]}e_y + w_{p,z[j]}e_z \tag{4.16}$$

4.3 Numerical methods

In order to perform the numerical simulation of the liquid-solid flow, we use the Computer Fluid Dynamics software ANSYS FLUENT 2021 (Matsson 2021). The present section describes the numerical methods used to perform the numerical simulation: the DDPM method, which can compute the effects of the continuous phase on the discrete phase; and the DEM method, which calculates the collision forces and torques originating from the collision between particles and between particle and solid surfaces.

Before performing the numerical simulation, a mesh of the problem geometry (Figure 4.3), must be created. The mesh finite elements have an average element size of 7.5×10^{-3} m. The tetrahedron method with patch conforming algorithm was used in the porous media zone (ANSYS meshing guide, 2010), as shown in Figure 4.5. A mesh resolution test can be found in Chapter 5. The number of elements is limited by the Students Licence of the Ansys Fluent to 512,000 elements.

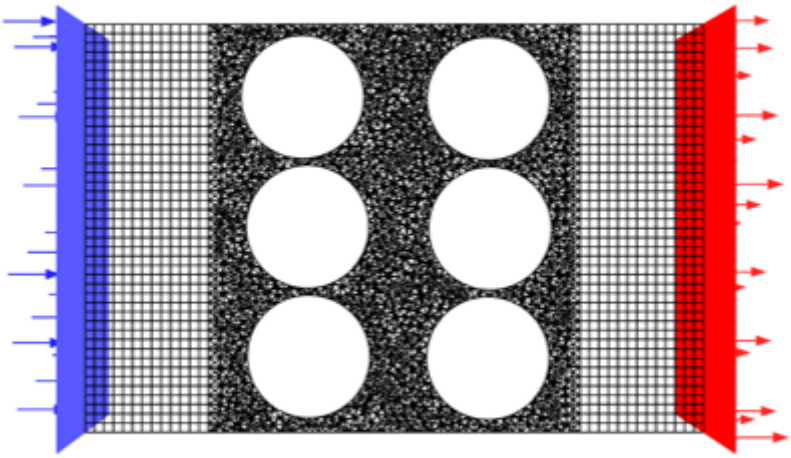

Figure 4.5: Mesh used to perform the numerical simulation on the problem geometry.

4.3.1 Dense Discrete Phase Method

The Discrete Phase Method (DPM) is a solution method for liquid-solid flow that considers the fluid as a continuous phase (Eulerian), with the flow field calculated through the Navier-Stokes equations. The solid particles are considered as

a disperse phase (Lagrangian), calculated using Newton's second law for each individual particle. The Dense Discrete Phase Method (DDPM), proposed by Popoff and Braun (2007), is an extension of the DPM method available on the ANSYS FLUENT program (Fluent manual, 2016) that enable us to obtain solutions in situations with a high concentration of particles, e.g. dense flow, ε_p>10%. The general form of the equations for the DDPM model for the conservation of mass and momentum for the continuous phase are expressed, respectively, by Equation (4.3) and Equation (4.4).

The F_{DPM} is the coupling term that incorporates the momentum exchange due to the movement of the discrete phase through every control volume of the continuous phase mesh, Equation (4.17). F_{DPM} is dependent of the particle mass flow rate $\dot{m}_p$ and the coupling coefficient $K_{p,f[j]}$ of the drag force C_d, Equation (4.18). S_{DPM} is the source term that computes the exchange of mass between phases in a determined control volume, as shown in Equation (4.19), where the subscript o means the outlet and the subscript i means the inlet.

$$F_{DPM} = \sum (K_{p,f}(u_p - u_f) + F_{\sigma p,f})\dot{m}_p \Delta t \tag{4.17}$$

$$K_{p,f[j]} = \frac{\varepsilon_f^{np} \rho_p C_{D[j]} Re_{p[j]}}{24\tau_{p[j]}} \tag{4.18}$$

$$S_{DPM} = -\sum \left(\frac{(m_p u_p)_o - (m_p u_p)_i}{\Delta t} \right) \tag{4.19}$$

Equation (4.20) represents the particle velocity, Equation (4.21) the particle position, and Equation (4.22) the particle angular velocity. $\tau_{p[j]}$ is the particle response time [s], Equation (4.23), dependent on the drag coefficient $C_{D[j]}$ and the particle's transnational Reynolds number $Re_{p[j]}$, Equation (4.24).

$$\frac{du_{p[j]}}{dt} = \frac{1}{\tau_{p[j]}}(u_{f[j]} - u_{p[j]}) + a_{pF[j]} \tag{4.20}$$

$$\frac{dx_{p[j]}}{dt} = u_{p[j]} \tag{4.21}$$

$$\frac{dw_{p[j]}}{dt} = \frac{T_{d,s[j]} + T_{c,s[j]}}{I_{p[j]}} \tag{4.22}$$

$$\tau_{p[j]} = \frac{24\rho_p d_{p[j]}^2}{18\mu_f C_{D[j]} Re_{p[j]}} \tag{4.23}$$

$$Re_{p[j]} = \frac{\rho_f d_{p[j]} |u_{p[j]} - u_{f,[j]}|}{\mu_f} \tag{4.24}$$

Equation (4.20) and Equation (4.21) are both solved numerically by implicit integration, as shown in Equation (4.25) and Equation (4.26). Equation (4.22) is solved by the trapezoidal method of Crank and Nicolson (1947), Equation (4.27).

$$u_{p,x[j]}^{n+1} = \frac{u_{p,x[j]}^{n} + \Delta t_p \left(a_{p,x[j]} + \frac{u_{f,x[j]}^{n}}{\tau_{p[j]}} \right)}{1 + \frac{\Delta t_p}{\tau_{p[j]}}} \tag{4.25}$$

$$x_{p,x[j]}^{n+1} = x_{p,x[j]}^{n} + \frac{1}{2}\Delta t_p (u_{p,x[j]}^{n+1} + u_{p,x[j]}^{n}) \tag{4.26}$$

$$w_{p,z[j]}^{n+1} = w_{p,z[j]}^{n} + \left(\frac{T_{d,s[j]} + T_{c,s[j]}}{I_{p[j]} \Delta t_p} \right)_{[j]} \tag{4.27}$$

Fluid velocity u_f is calculated on the stream line that crosses the centroid on particle [j], while $a_{pF[j]}$ is the particle acceleration by the sum of the forces described before, see Equation (4.5). The drag coefficient C_d and the Saffman lift force $F_{sl,s[j]}$ are described in Appendix C.

4.3.2 Discrete Elements Method

The Discrete Element Method (DEM), presented by Cundall and Strack (1979), computes the effects of the contact between particles and between particles and walls to the resulting force and torque. The calculation of the particle's movement is based on Newton's second law, in an individual scale of the particle (Dong *et al.* 2009). The contact between two particles happens in a finite area due to material deformation. In the present work the viscoelastic linear model (Kruggel-Emden *et al.* 2007), presented in Figure 4.6 as a spring-damper system, is applied. Therefore, the deformation can be approximated to the normal superposition δ_n, see Equation (4.28), dependent on the position of the particles centroid, $x_{p[j]}$ and $x_{p[i]}$, and diameters, $d_{p[j]}$ and $d_{p[i]}$.

$$\delta_{p[j]} = |x_{p[j]} - x_{p[i]}| - \frac{1}{2}(d_{p[j]} - d_{p[i]}) \tag{4.28}$$

Equation (4.29) presents the calculation for the resulting contact force for particle j, $F_{n[j]}$, which is dependent of the spring constant $k_{n[j]}$ [N/m] and the damper coefficient $\eta_{n[j]}$ $[N \cdot s/m]$, detailed in Appendix D. Applying Newton's third law to particle i results in the contact force $F_{n[i]}$, a force with same module but a different direction than $F_{n[j]}$, see Equation (4.30).

$$F_{n[j]} = -k_n \delta_n n_{[i,j]} - \eta_n (u_{[i,j]}.n_{[i,j]}) n_{[i,j]} \tag{4.29}$$

$$F_{n[i]} = -F_{n[j]} \tag{4.30}$$

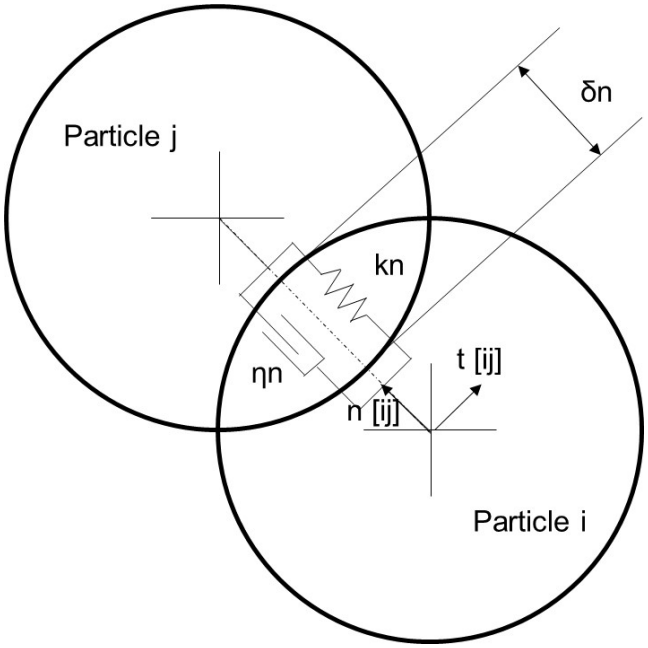

Figure 4.6: Visual representation of the mechanical model of spring and dumper to represent the superposition of particles j and i.

The relative velocity vector $u_{[ij]}$ and unitary normal vector $n_{[ij]}$ are calculated using Equation (4.31) and Equation (4.32). The spring constant $k_{n[j]}$ is estimated by Equation (4.33), assuming that the maximum superposition $\xi_{n[j]}$ is 0.27.

$$u_{[i,j]} = u_{p[i]} - u_{p[j]} \tag{4.31}$$

$$n_{[i,j]} = \frac{x_{p[i]} - x_{p[j]}}{|x_{p[i]} - x_{p[j]}|} \tag{4.32}$$

$$k_{n[j]} = \frac{\pi |u_{[i,j]max}|^2 d_{p[j]} \rho_{p[j]}}{3\xi_n^2} \tag{4.33}$$

The friction force $F_{f[i]}$ is calculated applying Coulomb friction law (Kruggel-Emden *et al.* 2007), Equation (4.34), using the friction coefficient, μ_f. By the Newton's third law the friction force in particle j, $F_{f[j]}$, is given by Equation (4.35).

$$F_{f[i]} = \mu_f |F_{n[i]}| t_{[i,j]} \tag{4.34}$$

$$F_{f[j]} = -F_{f[i]} \tag{4.35}$$

The unitary vector, $t_{[ij]}$, is calculated by Equation (4.37), based on the the relative velocity of the particle approximation on the tangential direction $u_{t[ij]}$, Equation (4.36),

$$u_{t[ij]} = u_{[ij]} - (u_{[ij]} \cdot n_{[ij]}) n_{[ij]} \tag{4.36}$$

$$t_{[ij]} = \frac{u_{t[ij]}}{|u_{t[ij]}|} \tag{4.37}$$

The collision torques between particles i and j are calculated after defining the collision and friction forces. Torque due to normal force in particle i, $T_{n[i]}$, is a function of the friction force $F_{f[i]}$, Equation (4.38), and to calculate the torque due to normal force in particle j $T_{n[j]}$, Newton's third law is used, according to Equation (4.39). Torque due to tangential force in particle i, $T_{t[i]}$, results from rolling friction and is described as a function of the rolling friction coefficient μ_r [-], detailed in Appendix D, and the angular velocity of the particle $w_{p[j]}$, according to Equation (4.40), and to find the torque due to the tangential force in particle j, $T_{t[j]}$, the third law of Newton used, as shown in Equation (4.41).

$$T_{n[i]} = \frac{d_{p[i]}}{2} n_{[ij]} * F_{f[i]} \tag{4.38}$$

$$T_{n[j]} = -T_{n[i]} \tag{4.39}$$

$$T_{t[i]} = -\mu_r |F_{n[i]}| \frac{w_p[i]}{|w_p[i]|} \tag{4.40}$$

$$T_{t[j]} = -T_{t[i]} \tag{4.41}$$

4.3.3 Numerical solution flow chart

Figure 4.7 presents the iteration flow chart of the interactive numerical method DDPM-DEM. First occurs the monophasic flow simulation of fluid to determine the pressure and velocity fields. When the fluid velocity is calculated, the particles are injected into the numerical domain through the injection points at each fluid time steep. Then it calculates the position $x_{p[j]}$, velocity $v_{p[j]}$ and angular velocity $w_{p[j]}$ of the particle j. For the computation of forces and torques, it uses the equations in Table 4.1. If it is a collision between particles or between particles and surface, the DEM method is applied. Because the acceleration $a_{p[j]}$ is a function of the velocity $v_{p[j]}$, every time step is updated with the new value of velocity, which is also corrected on the next step by the new acceleration value. Such a process is repeated for a predetermined number of interactions for the solid particles in the domain.

Once all particles have their values of position $x_{p[j]}$, velocity $v_{p[j]}$ and rotation $w_{p[j]}$ are adequately computed, the volumetric fluid fraction and source terms ε_f^{np}, s_{DPM}^{np} and f_{DPM}^{np} are then calculated for each control volume of the computational mesh. With such values, the flow solution is performed via the Finite Volume Method using of the pressure correction method (Pressure-Based

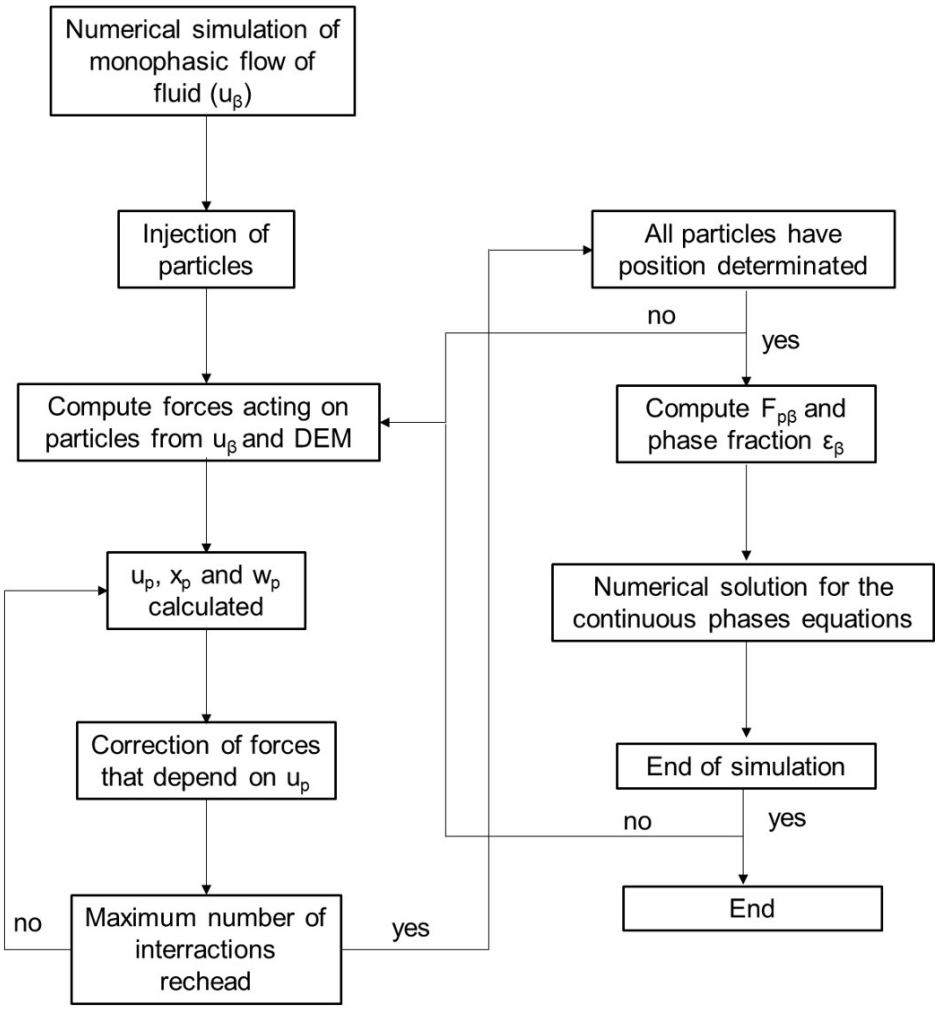

Figure 4.7: Fluxogram for the numerical solution of the hybrid method DDPM-DEM.

Solver) of segregated form (Chorin 1968). The gradients are computed using the method of least squares based on the center of the computational control volume (Least Squares Cell-Based) using the Gram-Schmidt process (W. K. Anderson and Bonhaus 1994). Advective terms (momentum and volume fraction) are analyzed using the second order upwind method (S. V. Patankar 2018). The continuous phase pressure field P_f [Pa] is determined based on the velocity components $u_{f,x}$ and $u_{f,y}$ applying the coupling method PC-SIMPLE (Phase-coupled Semi-Implicit Method for Pressure Linked Equations) (Vasquez 2000), which is an adaptation of the pressure-velocity coupling SIMPLE (S. V. Patankar and Spalding 1983) for multi-phase flows.

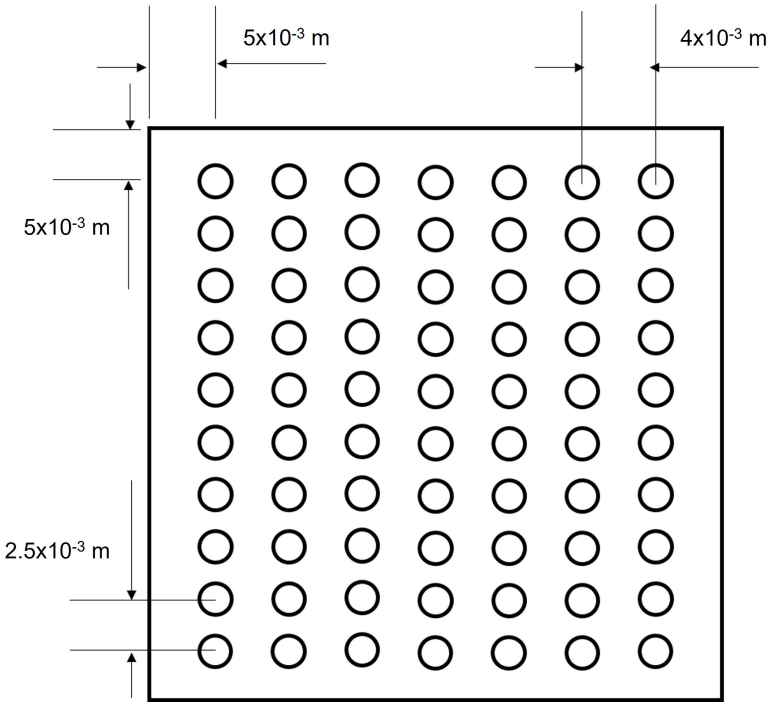

Figure 4.8: Illustration of the injection surface.

4.4 Particle injections

The particles are injected in the computational domain with an initial velocity u_{inj} [m/s] through a surface of injection points (n=70), as illustrated in Figure 4.8. The injection surface is located 5×10^{-3} m from the inlet surface, to decrease the wall effect in the solid particles. The $\dot{m}_{inj}$ [kg/s] is calculated by Equation (4.42), based on the diameter of the particle d_p [m], the number of injection points n_{inj}, the specific mass of the particle ρ_p [kg/m^3] and the injection time step Δt_{inj} [s].

$$\dot{m}_{inj} = \frac{n_{inj}}{\Delta t_{inj}} \rho_p \frac{4\pi}{3} \left(\frac{d_p}{2} \right)^3 \tag{4.42}$$

For the injection of particles, it must be ensured that there is no overlapping particles, therefore, a restriction must be imposed so a particle injected at time $n+1$ does not overlap with the one injected at the previous time n. This restriction is given by Equation (4.43). The solid particles are injected into the domain at every time step of the fluid.

$$\Delta t_{inj} > \frac{d_p}{|u_{inj}|} \tag{4.43}$$

Chapter 5

Results and discussion

This chapter presents the results regarding the process of clogging a porous medium under dynamic filtration conditions to combat loss of circulation. The proposed numerical parameters related to DDPM-DEM are listed in Table 5.1. The fluid has specific mass of ρ_f=1188 [kg/m^3] and viscosity of μ_f=2.797×10^{-2} [kg/(m·s)]. The parameters analysed are the solid particle flow rate $\dot{n}_{part}$ $[n_{part}/s]$, fluid velocity in the outlet surface $v_{f,o}$ $[m/s]$, fluid volumetric flow rate at the outlet surface $Q_{f,o}$ $[m^3/s]$, and normalized fluid flow rate at the outlet surface (q_f) [-]. The parameter, q_f, is a normalization of the $Q_{f,o}$(t) parameter, divided by the value when the fluid flow reaches a steady flow, $Q_{f,o}$(t=1s), see Equation (5.1). The preliminary results presented in this chapter are based on the author's previous project report.

$$q_f = \frac{Q_{f,o}(t)}{Q_{f,o}(t = 1s)} \tag{5.1}$$

Table 5.1: Summary of the numerical parameters.

Parameter	Symbol	Value	Unit
Time step of discreet phase	Δt_p	10^{-4}	[s]
Time step of continuous phase	Δt_f	10^{-2}	[s]
Injection points	N_p	70	[-]
Spring dashpot constant	k	25	[N/m]
Particle-particle restitution coefficient	η_p	0.9	[-]
Particle-wall restitution coefficient	η_p	0.6	[-]
Static friction coefficient	μ_s	0.05	[-]
Glide friction coefficient	μ_g	0.02	[-]
Limit friction coefficient	μ_l	0.01	[-]

Table 5.2: The effect of mesh refinement on the simulation results.

Parameter	Mesh 1	Mesh 2	Mesh 3	Mesh 4
s_{ele} [m]	10^{-3}	0.85×10^{-3}	0.75×10^{-3}	0.7×10^{-3}
n_{ele} [elements]	173,964	280,783	403,181	495,266
$Q_{f,o}$ [m^3/s]	1.42×10^{-6}	1.38×10^{-6}	1.36×10^{-6}	1.36×10^{-6}
ΔP [Pa]	9.933	9.935	9.9355	9.936
K [m^2]	1.171×10^{-7}	1.138×10^{-7}	1.121×10^{-7}	1.119×10^{-7}

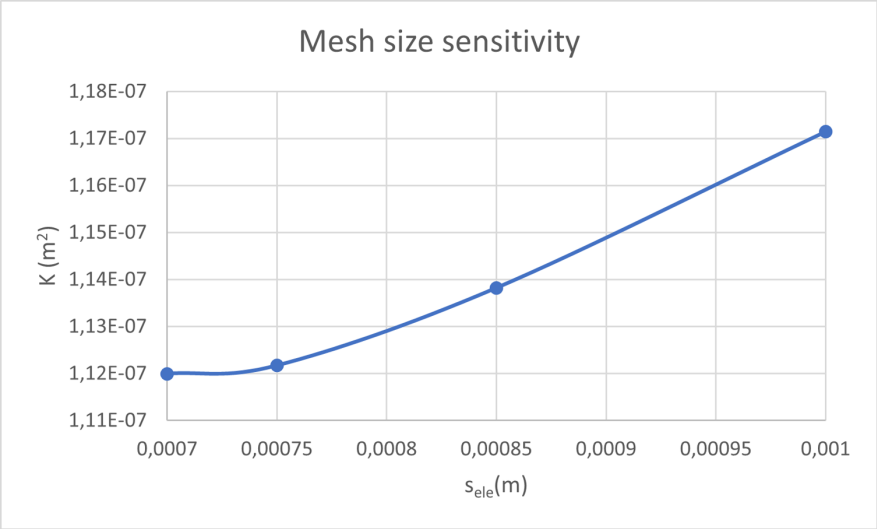

Figure 5.1: The obtained permeability for different mesh sizes s_{ele}.

5.1 Preliminary results

5.1.1 Mesh size sensitivity

The mesh size sensitivity test for the sphere pack section was performed by simulating a single-phase liquid flow. It is applied a pressure difference of ΔP= 10 Pa as boundary condition in the geometry presented in Figure 4.3. The present test analyses the effect of elements in the domain n_{ele} [-] in parameters such as volumetric flow rate at the outlet $Q_{f,o}$ [m^3/s], pressure difference in the porous media ΔP [Pa] and permeability K [m^2], all presented in Table 5.2.

Figure 5.1 is a plot of the calculated permeability, using Equation (3.3), versus the average element size of the mesh, s_{ele}, calculated using Equation (3.3). It is possible to see that when reducing s_{ele}, k tends to converge to a stable value. For the further simulations of the present work, we used an element size of 0.75×10^{-3} m. It was observed a permeability difference of approximately 0.2%, compared with a mesh of element size of 0.7×10^{-3}m. This was deemed acceptable, giving the reduced computational need when using a coarse grid.

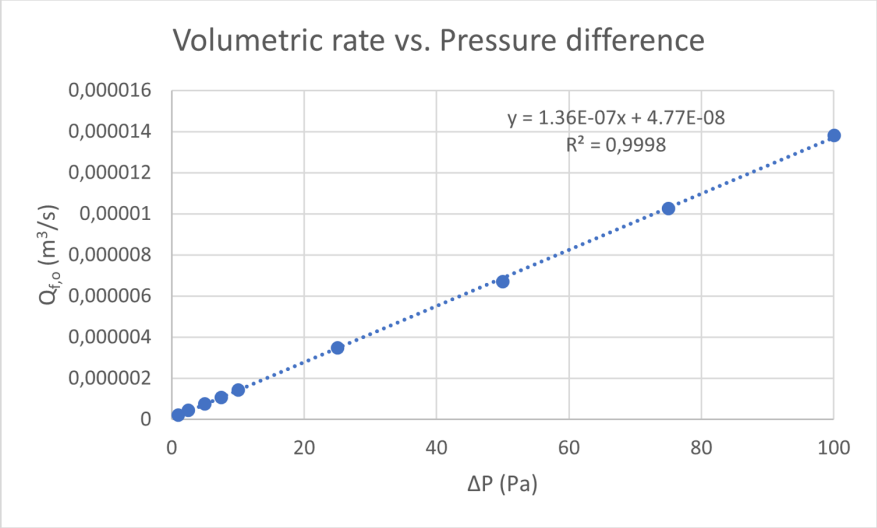

Figure 5.2: Plot of the fluid volumetric flow rate at the outlet $Q_{f,o}$ in relation to pressure difference ΔP.

5.1.2 Single-phase flow simulation in the porous media

Before the injection of particles in the domain, we analysed a single-phase fluid flow. The volumetric flow rate at the outlet surface $Q_{f,o}$ is observed for the different pressure differencesΔP=1; 2.5; 5; 7.5; 10; 25; 50; 75; 100 Pa.

Figure 5.2 shows the results for $Q_{f,o}$ versus ΔP. The coefficient of determination between the two parameters is an almost linear equation, with an R^2=0.9998. We also observed that the cross-over with the x-axis is approximately zero, in accordance with the theory.

The slope of the linear equation presented in Figure 5.2 gives $Q_{f,o}/\Delta P$. The Darcy law, Equation (3.2), is applied to determinate the permeability of the porous medium considering the viscosity as μ_f [N·s/m^2], this gives K$\approx 1.12\times10^{-7}$ m^2. The permeability result was compared with the permeability calculated using the Kozeny-Carman equation, Equation (5.2).

$$K = \frac{\phi^3 d^2}{36k(1-\phi)^2} \tag{5.2}$$

Here K is the permeability [m^2], ϕ is the porosity of the porous medium [-], d is the diameter of the sphere in the packing [m], and k is the empirical Kozeny Carman constant. For beds packed with spherical particles, k is approximated to be 5 (P. Xu and B. Yu 2008). The permeability estimated from the Kozeny-Carman equation gives 3.11×10^{-7} m^2, which is a value relatively close to the one found in our simulations.

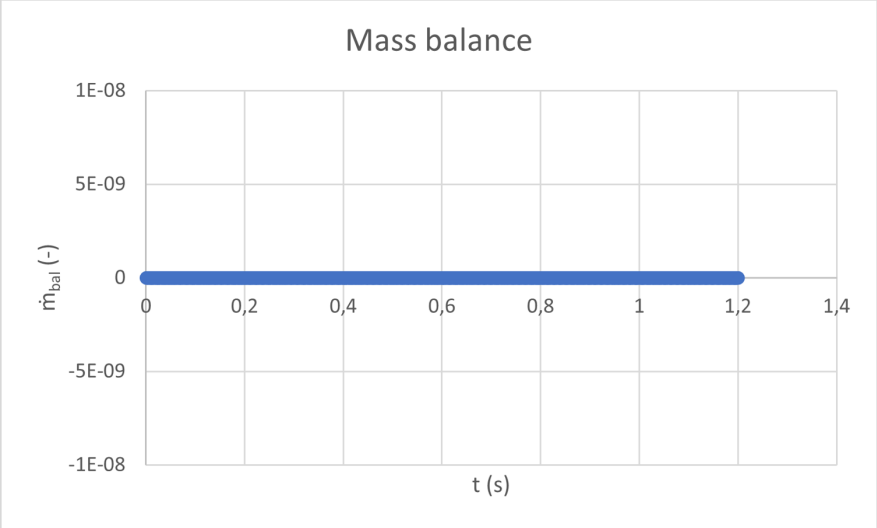

Figure 5.3: Test of the mass balance of particles $\dot{m}_{bal}$.

5.1.3 Mass balance

A mass balance test of the particles inside the domain was performed to ensure that the Ansys software makes the right calculations for the liquid-solid flow. The solid particles used in this test have specific mass of ρ_p=1550 kg/m^3 and diameter of d_p=2×10^{-3} m.

Figure 5.3 shows the plot for the mass balance of solid particles in the domain, following the equation presented in Equation (5.3). Considering $\dot{m}_{bal}$ is the mass change per unit of time of the particles, $\dot{m}_{esc}$ is the mass of particles that escaped the domain per unit of time, $\dot{m}_{cv}$ is the mass of particles trapped in the domain per unit of time, and $\dot{m}_{inj}$ is the mass of particles injected in the domain per unit of time. The injection of particles starts at t=0.6 s and stops at t=1.0 s. The plot of $\dot{m}_{bal}$ is a straight line with a value equal to zero, indicating that the sum of particles leaving the system plus the particles inside the system is the same as the particles been injected in the system. The plot of Figure 5.3 is in agreement with Equation (5.3), concluding that the CFD-DEM model successfully reproduces the mass balance of particles of a liquid-solid flow.

$$\dot{m}_{bal} = -\dot{m}_{esc} - \dot{m}_{cv} + \dot{m}_{inj} = 0 \tag{5.3}$$

5.1.4 Liquid-solid flow

In order to study the the numerical method DDPM-DEM, a simple liquid-solid flow is simulated. Solid particles, ρ_p=1550 kg/m^3 and diameter of d_p=0.5×10^{-3} m, are injected in a horizontal square channel (3.2; 3.2; 5×10^{-2} m) from t=2 s to t=2.5 s.

Figure 5.4 presents the solid particles flow rate $\dot{n}_{part}$ [n_{part}/s] as a function

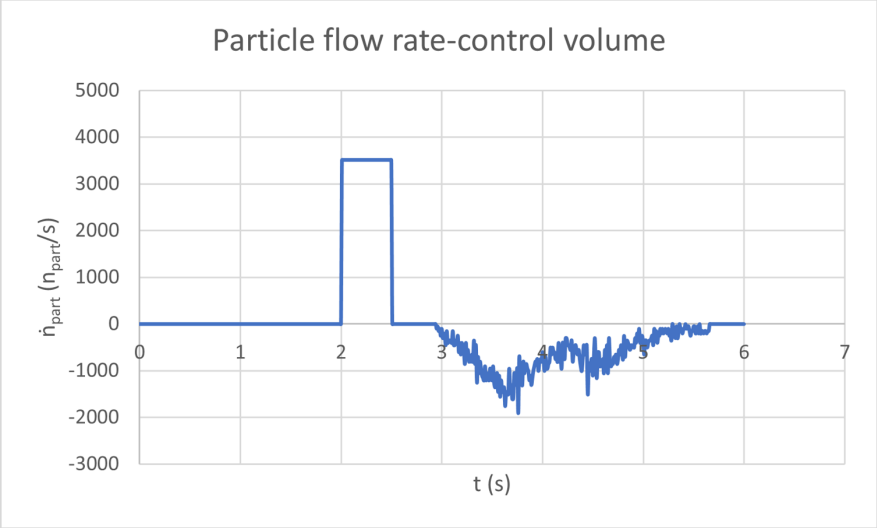

Figure 5.4: Plot of solid particle flow rate $\dot{n}_{part}$ versus time t, of a liquid-solid flow.

of time t. It is visible at the mark of t=2 s a peak of $\dot{n}_{part}$ when the solid particles are injected, and $\dot{n}_{part}$ drops at t=2.5 s when the injection stops. At the mark of approximately t=3 s, the $\dot{n}_{part}$ starts a negative trend because the solid particles are beginning to leave the channel. Due to the boundary effects of the walls, the particles in the center of the channel have more velocity than the ones near the border. This explains why some particles exit the domain sooner, and others take longer to leave.

Figure 5.5 shows the fluid velocity in the outlet surface $v_{f,o}$ [m/s] as a function of the time. The injection of the solid particles happens after the fluid flow reaches a stable condition. As the solid particles are injected into the domain, the $v_{f,o}$ decreases. When the injection of particles stops, the $v_{f,o}$ reaches a plateau. When the solid particles start leaving the domain, the $v_{f,o}$ begins to rise. Finally, when all particles are out of the domain, the $v_{f,o}$ is back to the stable condition it was before the injection.

5.1.5 Liquid-solid flow in porous media

This subsection studies the effects of the injection of solid particles in the fluid flow in our porous medium. The solid particles used have ρ_p=1550 kg/m^3 and diameter of d_p=1.5×10^{-3} m. A boundary condition of ΔP=10 Pa is defined. A single-phase flow is simulated until t=1 s, and then the injection of particles occurs for 0.5 s, and finally, the simulation stops at t=15 s.

Figure 5.6 presents the particle flow rate $\dot{n}_{part}$ [n_{part}/s] for the liquid-solid flow simulation in porous media. The curve starts at $\dot{n}_{part}$=0 n_{part}/s, since the flow starts as single phase. When the simulation reaches t=1 s, the curve jumps to $\dot{n}_{part}$=7500 n_{part}/s, indicating the beginning of the particle injection. The solid

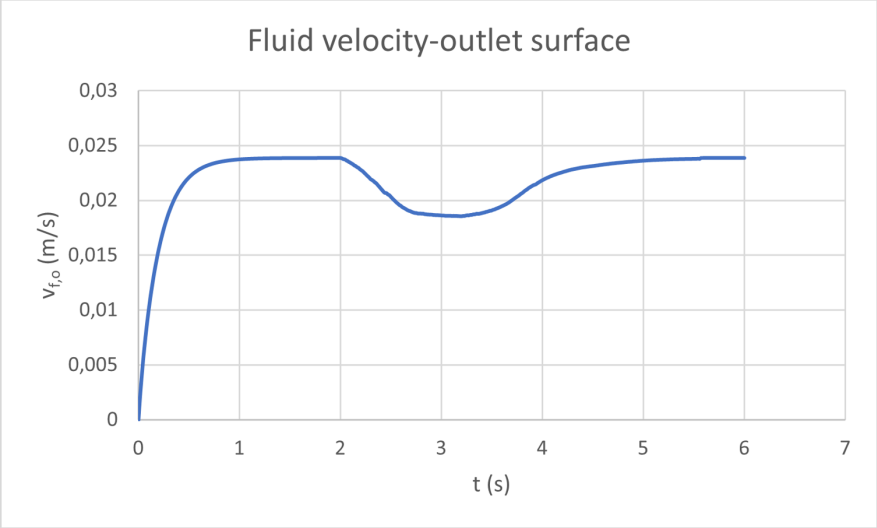

Figure 5.5: Plot of the fluid velocity in the outlet surface $v_{f,o}$ versus time t, of a liquid-solid flow.

particles are stopped being injected at t=1.5 s, as seen in the curve returning to approximately zero. Nonetheless, it is possible to see oscillations in the plot in the period t=1-2.5 s, suggesting the exit of some solid particles through the inlet surface. The curve presents a flat behavior until t=12.5 s, where the oscillation may indicate an escape of some particles trapt in the porous media through the outlet surface.

Figure 5.7 shows the average fluid velocity on the outlet surface $v_{f,o}$ for the liquid-solid flow simulation in porous media. At t=1 s, when the solid particles are injected into the system, the curve has a jump in $v_{f,o}$. Since the mixture in the domain becomes denser, the fluid increases the velocity to carry the particles and keep the boundary conditions. After the injection of particles stops and the particle filter starts forming, a decreasing trend is perceptible, indicating that the filter reduces the fluid flow. At t=10 s the curve reaches a stable level.

Figure 5.8 plots the normalized fluid flow rate at the outlet surface q for the liquid-solid flow simulation in porous media. When the particles are injected in the domain, is visible that q has a peak, indicating that approximately 1.6 times more volume of fluid is exiting through the outlet surface than when simulating a single-phase flow. When the particle filter starts forming, q starts reducing, until it reaches a new steady-state equal to 77% of the initial q value.

Figure 5.9 shows the clogging process in the domain at t=15 s for the liquid-solid flow simulation, with 2288 particles inside the domain. It is possible to see that some solid particles are starting to leave the domain through the outlet surface, in agreement with the plot of Figure 5.6. While the particle filter inside the porous medium starts dissolving, the particle filter at the inlet of the porous medium is still stable.

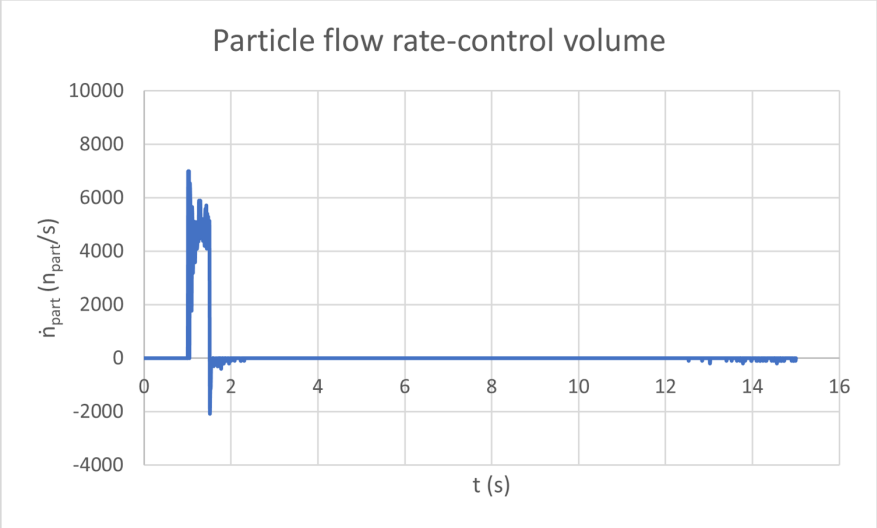

Figure 5.6: Plot of solid particle flow rate $\dot{n}_{part}$ versus time t, of a liquid-solid flow in porous media.

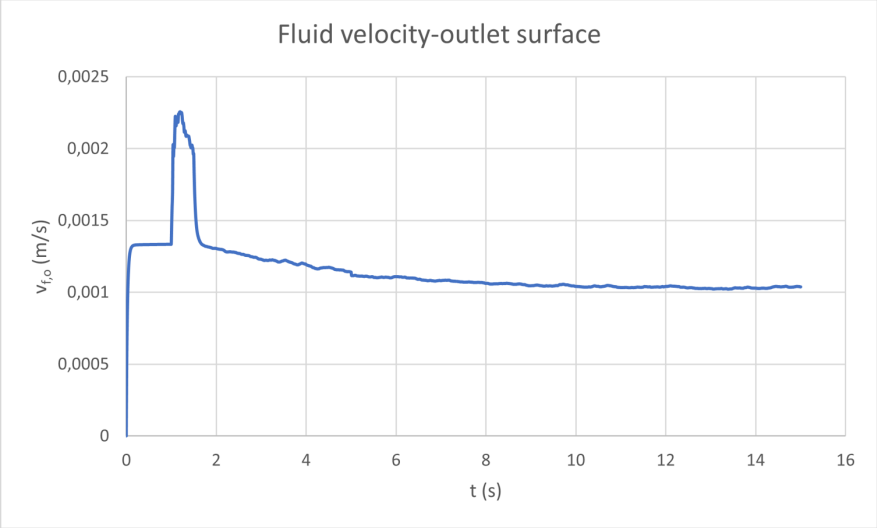

Figure 5.7: Plot of the fluid velocity in the outlet surface $v_{f,o}$ versus time t, of a liquid-solid flow in porous media.

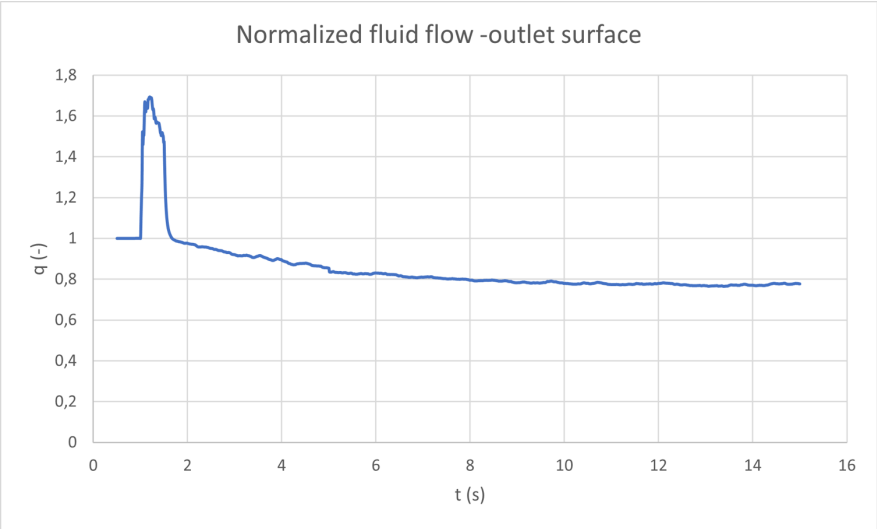

Figure 5.8: Plot of the normalized fluid flow rate at the outlet q_f versus time t, of a liquid-solid flow in porous media.

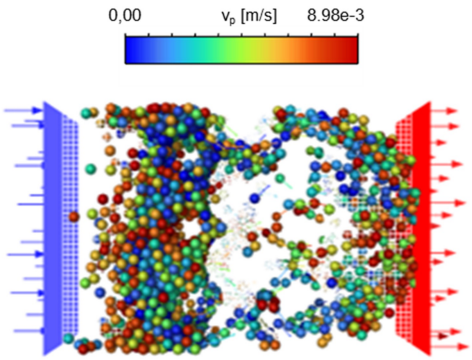

Figure 5.9: Filter formation at t=15 s of a liquid-solid flow in porous media.

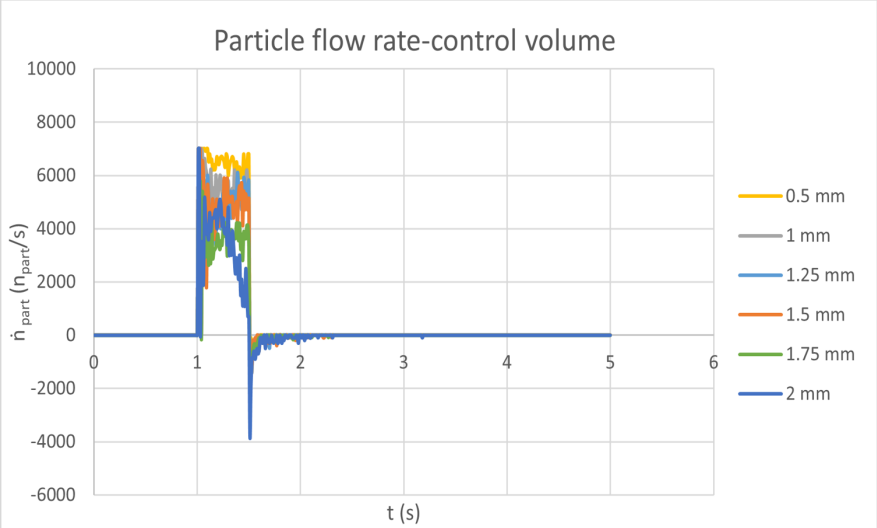

Figure 5.10: Plot of the solid particle flow rate $\dot{n}_{part}$ versus time t, analysing particle diameter d_p.

5.2 Particle proprieties

The present section of the project evaluates the effects on the clogging process by varying the solid particle's proprieties. The proprieties analyzed are: particle diameter, particle-fluid density ratio, and combination of multiple particles.

5.2.1 Particle diameter

In this section the effects of the variation of the particles diameter, d_p=(0.5; 1; 1.25; 1.5; 1.75; 2×10^{-3} m), is evaluated. The specific mass is kept constant at ρ_p=1550 kg/m^3. The simulation started with single-phase fluid flow in the domain, reaching a steady state. At t=1 s, the injection of solid particles starts. The particles stop being injected at t=1.5 s.

Figure 5.10 presents the particle flow rate $\dot{n}_{part}$ [n_{part}/s]. Different from Figure 5.4, the $\dot{n}_{part}$ curves present some interference during the injection phase. The inlet and injection surface is close to the porous medium, so when there is a collision between particles or between a particle and the porous medium, some particles can exit through the inlet surface. The larger the d_p, the lower is the $\dot{n}_{part}$ during the injection phase. This happens due to the fact that particles with a larger diameter can form the mud cake filter faster, so more particles escape the domain through the inlet surface.

Figure 5.11 plots the average fluid velocity at the outlet surface $v_{f,o}$. The injection of solid particles generates an acceleration of the fluid in the system during the period of injection. The larger the d_p, the higher the $v_{f,o}$ gets during the injection phase. For the cases with $d_p \geq 1.5\times10^{-3}$ m, during the injection phase, $v_{f,o}$ decreases before the injections stop. This is probably due to the early formation of

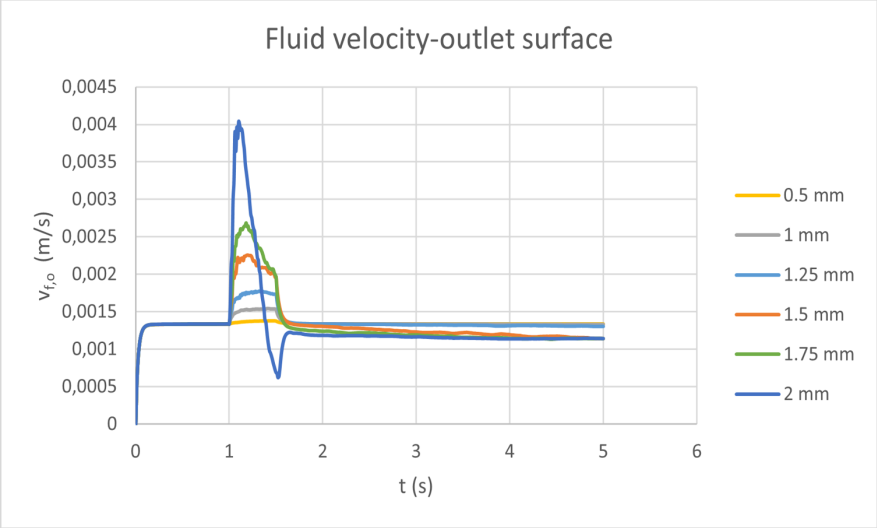

Figure 5.11: Plot of the fluid velocity at the outlet surface $v_{f,o}$ versus time t, analysing particle diameter d_p.

the filter. In the case with $d_p = 2\times10^{-3}$ m, $v_{f,o}$ is reduced below to the steady state level $v_{f,o}$(t=1s), causing the fluid to return through the inlet surface. For the cases of $d_p \geq 1.5\times10^{-3}$ m, it is a visible trend of decreased in $v_{f,o}$ before the injection of particles is finish. Indicating the occurrence of clogging. The same effect is not seem for the cases with $d_p \leq 1.25\times10^{-3}$ m. Indicating that even if the particles are still in the system, they do not form an effective particle filter.

Figure 5.12 plots the normalized fluid flow rate at the outlet surface q [-]. The behavior of the q presents the same trends as the ones seem in Figure 5.11, for the $v_{f,o}$. After the start of the solid particles injection, there is a increase in the q of all cases due the increase in fluid velocity $v_{f,o}$ follow by a decrease in q after the injection of particles stop. For the cases with $d_p \leq 1.25\times10^{-3}$ m, the value of q in the end of the simulation is very similar to the value in the steady state. For the cases with $d_p \geq 1.5\times10^{-3}$ m, a reduction of q is seen, indicating the effectiveness of the clogging process. For the simulation with $d_p = 2\times10^{-3}$ m, a drastic increase in q is seen when the injection process starts follow by an abrupt decrease in q. One possibility is that the sudden change in the density of the mixture causes the flow to become turbulent, generating vortexes near the inlet surface due to the accumulation of particles. The particle size of $d_p = 2\times10^{-3}$ m is the least recommended solution, because during the process of well drilling a sudden change in q can cause damage to the rock formation.

Table 5.3 presents the volume occupied by the solid particlesin the domain (V_p) after 5 seconds of simulation. It is noticeable that the larger the d_p, the higher is the total volume of particles in the domain. Larger particles can form the particle filter faster, making it difficult for new particles to settle in the system. The final results for $Q_{f,o}$ is be seen in Table 5.3. Considering $Q_{f,o}$(t=1)$=1.450\times10^{-6}$ m^3/s,

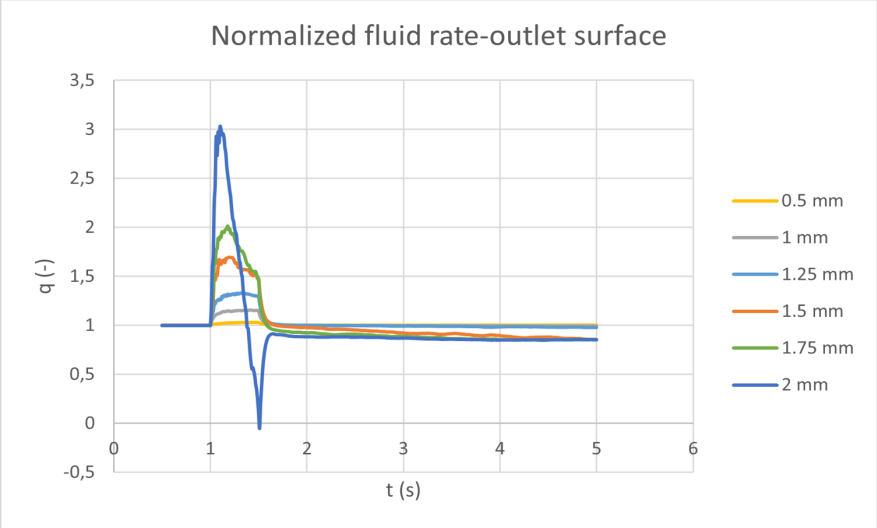

Figure 5.12: Plot of the normalized fluid flow rate at the outlet q versus time t, analysing particle diameter d_p.

Table 5.3: Results for V_p [m^3], $Q_{f,o}$ [m^3/s] and q [-] after 5 seconds of simulation for the variation of particle diameter d_p.

d_p [m]	$Q_{f,o}$ [m^3/s]	q [-]	V_p [m^3]
0.0005	1.450×10^{-6}	1.00	2.121×10^{-7}
0.001	1.442×10^{-6}	0.99	1.415×10^{-6}
0.00125	1.414×10^{-6}	0.97	2.494×10^{-6}
0.0015	1.238×10^{-6}	0.85	4.097×10^{-6}
0.00175	1.238×10^{-6}	0.85	5.936×10^{-6}
0.002	1.238×10^{-6}	0.85	6.473×10^{-6}

the final value for q can be calculated. For the cases with $d_p \geq$ 1.5 mm, the final value of q is around 0.85, indicating that the clogging process reduced the permeability of the system. Utilizing particles smaller than d_p=1.5×10^{-3} m don't seen to effectively reduce q, as seen in Figure 5.13. Using particles larger than d_p=1.5×10^{-3} m also do not seen viable, since the final result for q is very similar but demand more fluid velocity v_f to be carried.

Figure 5.14 shows the clogging process in the domain at t=5 s for the different particles size d_p. For the cases of d_p=0.50; 1.00; 1.25×10^{-3} m, the particles are still very dispersed in the fluid. In the other hand, for the cases d_p=(1.50; 1.75; 2.00×10^{-3} m), it is visible a well formed cluster of particles outside the porous medium, forming a filter. For the case d_p=2.00×10^{-3} m, the particles have a low penetration to the porous medium. The velocity of the particles v_p increase considerably with the increase of d_p, in agreement with the increase of fluid velocity $v_{f,o}$ seen in Figure 5.11, that carries the particles.

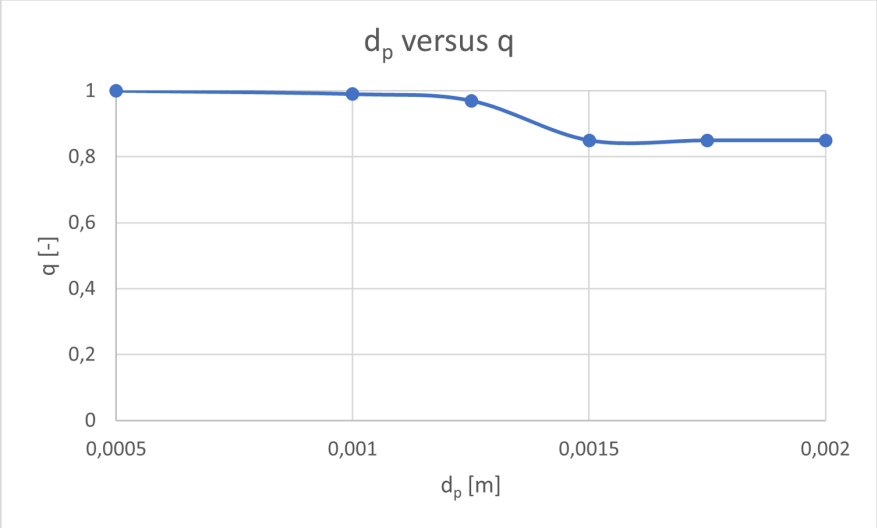

Figure 5.13: Plot of the final normalized fluid flow rate at the outlet q versus particle diameter d_p.

Table 5.4: Examples of Lost Circulation Materials, with $\rho_f = 1188(kg/m^3)$

Material	ρ_p [kg/m^3]	$\rho_p/(\rho_f$ [-]	Reference
NaCl polymer	1280	1.08	Amanullah (2016)
Plastic abrasives	1550	1.30	Souza Fritoli *et al.* (2021)
Glass beads	2540	2.14	Kim *et al.* (1996)

5.2.2 Particle-fluid density ratio

This section analyzes the influence of the particle-fluid density ratio ρ_p/ρ_f in the clogging process in our sphere pack. The fluid specific mass is constant at ρ_f=1188 kg/m^3, while the material of the particles is changed. Several different materials can be used as LCM, the ones considered in this work are shown in Table 5.4. The particle diameter, d_p=1.5×10^{-3} m, is constant for all simulations. First, only the fluid flow is simulated until it reaches a steady state. The particles are then injected into the domain between t=1-1.5 s, with the simulation continuing until t=5 s.

The particle flow rate $\dot{n}_{part}$ $[n_{part}/s]$ is presented in Figure 5.15. It is noticeable that the three different types of particles have similar behaviors. Particles with higher ρ_p/ρ_f have a slightly higher tendency to escape through the inlet surface before forming the mud cake filter. Particles with higher ρ_p/ρ_f also present less oscillation in the plot after the end of the particle injection, indicating a more stable filter formation with fewer particles escaping the domain.

The average fluid velocity on the outlet surface $v_{f,o}$ [m/s] is plotted in Figure 5.16. It is visible that the cases with higher ρ_p/ρ_f have higher velocity pecks during the injection of particles. This phenomenon occurs because heavier particles

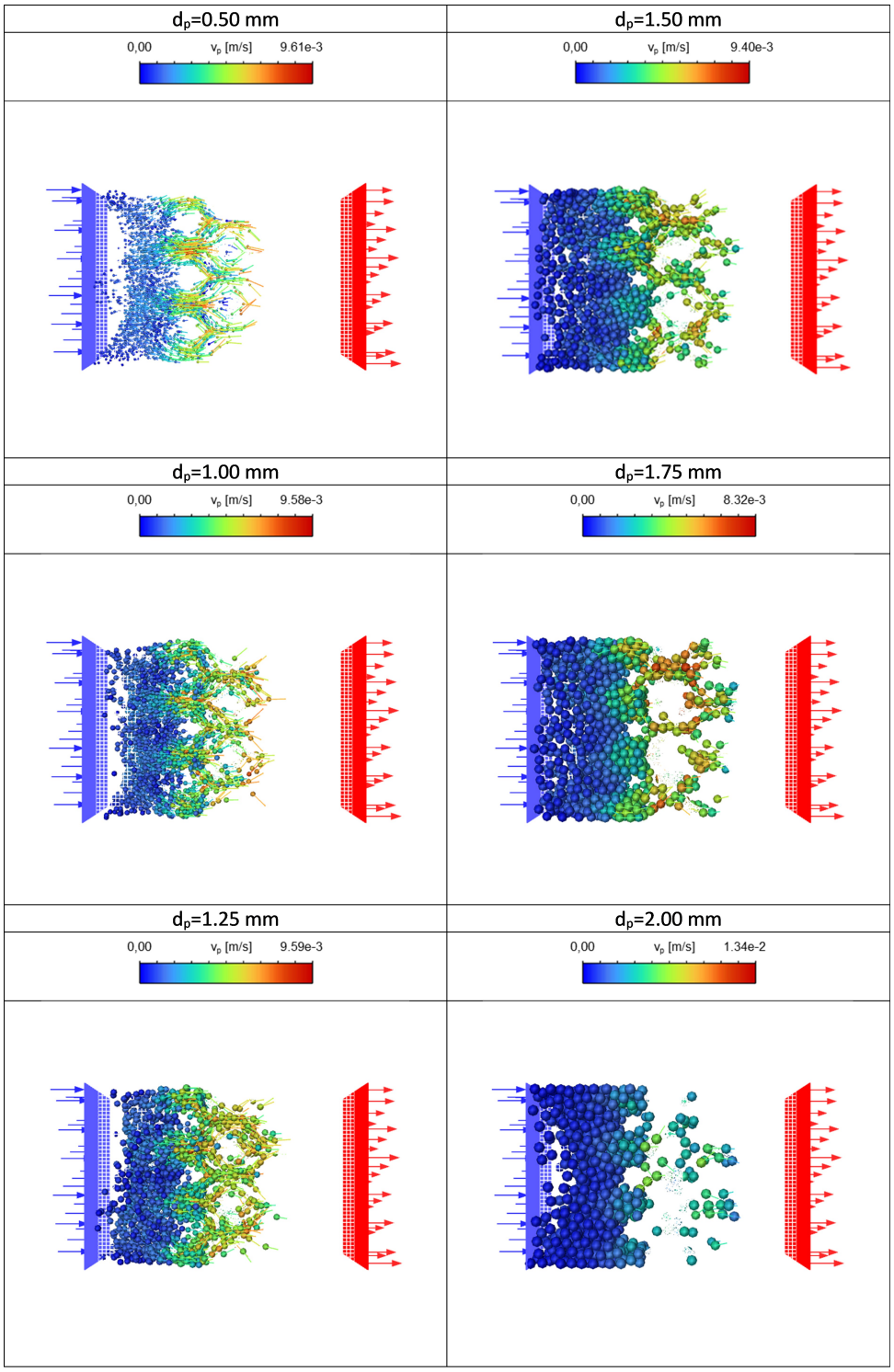

Figure 5.14: Filter formation at t=5 s, analysing the variation of particle diameter d_p.

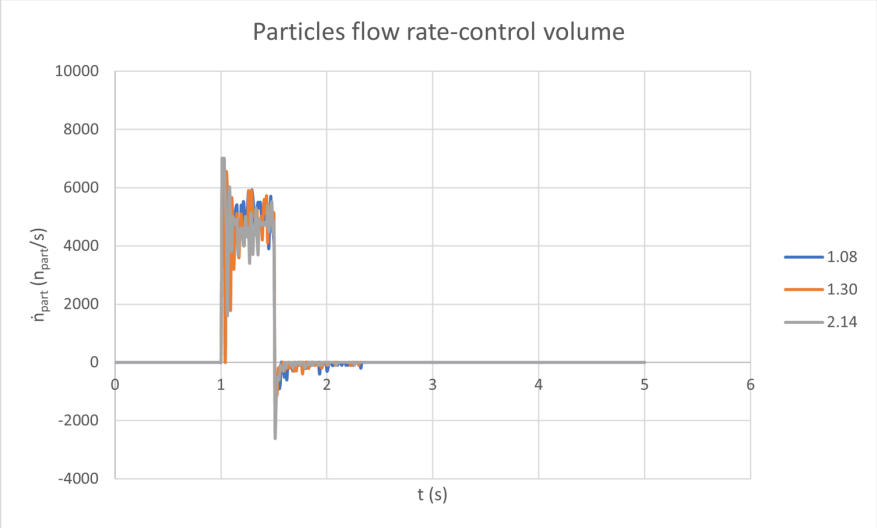

Figure 5.15: Plot of the solid particle flow rate $\dot{n}_{part}$ versus time t, analysing particle-fluid density ratio ρ_p/ρ_f.

demand that the fluid have more velocity to carry the particles. After the end of the injection of the particles and the formation of the particle filter, all cases present similar values for $v_{f,o}$. Cases with higher ρ_p/ρ_f presenting a slightly lower value for $v_{f,o}$.

The normalized fluid flow rate at the outlet surface q [-] is plotted in Figure 5.17. During the particles injection phase, the cases with higher ρ_p/ρ_f present higher q. Indicating that heavier particles demand higher fluid flow in the same boundary conditions. In this plot is visible that all cases appear to have the same behavior for q after the filter formation. Particles with higher ρ_p/ρ_f are thus considered the worst combative measure because they demand a larger increase in q in the initial phase and do not provide a better retention filter.

The volume occupied by the solid particles V_p for all cases at t=5 s are presented in Table 5.5. We observe that the difference in V_p between the three cases is small, but particles with higher ρ_p/ρ_f have slightly fewer particles in the domain. The final results for $Q_{f,o}$ is be seen in Table 5.5. Considering $Q_{f,o}$(t=1)=1.450×10^{-6} m^3/s, the final value for q can be calculated. All cases give similar results, of approximately 85% of the initial q, indicating that changing the ρ_p/ρ_f of particles is not an effective countermeasure to combat lost circulation. In Figure 5.18 is possible to see an almost straight line for the final results for q versus ρ_p/ρ_f.

Figure 5.19 shows the final result for the clogging process in the domain for the variations in ρ_p/ρ_f at t=5 s. It is visible that variations in ρ_p/ρ_f do not present great changes in the filter formed by the solid particles. All cases have similar levels of particle penetration in the porous medium and filter thickness. The velocity of the particles v_p increases slightly with the increase of $\rho_p/(\rho_f$, due to an increase in fluid velocity.

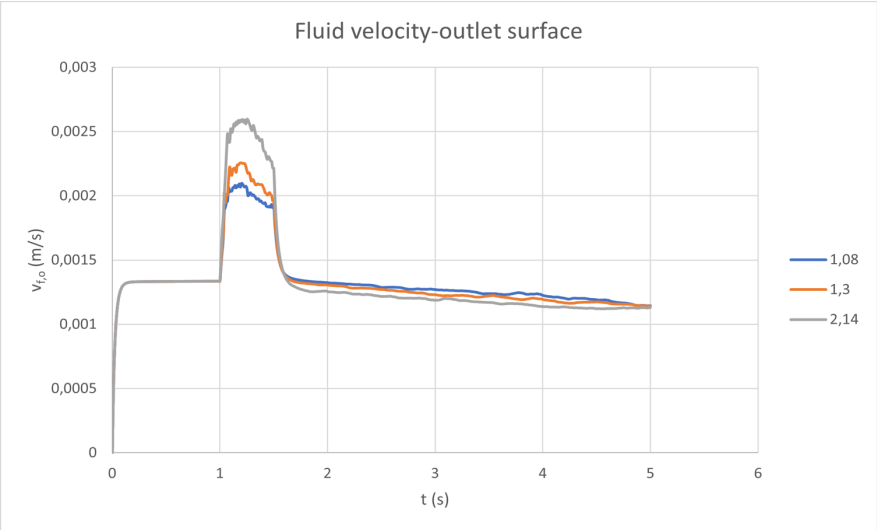

Figure 5.16: Plot of the fluid velocity at the outlet surface $v_{f,o}$ versus time t, analysing particle-fluid density ratio ρ_p/ρ_f.

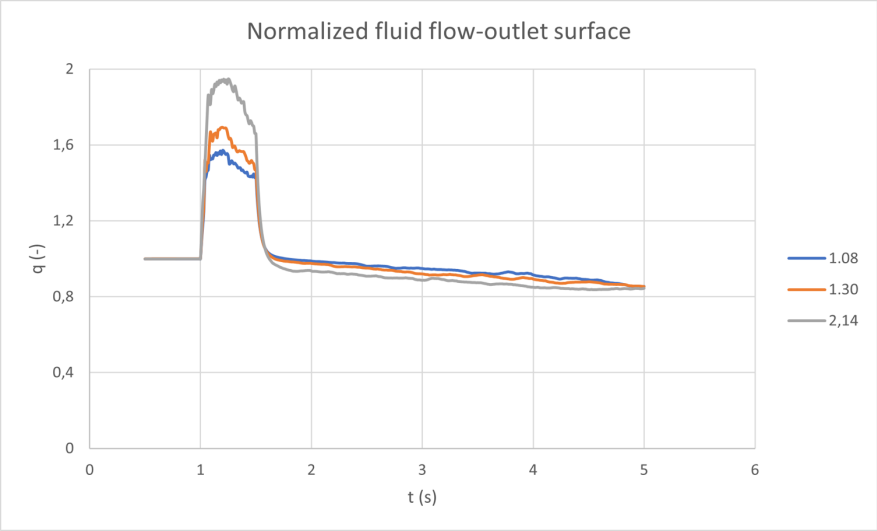

Figure 5.17: Plot of the normalized fluid flow rate at the outlet q versus time t, analysing particle-fluid density ratio ρ_p/ρ_f.

Table 5.5: Results for V_p [m^3], $Q_{f,o}$ [m^3/s] and q [-] after 5 seconds of simulation for the variation of particle-fluid density ratio ρ_p/ρ_f.

ρ_p/ρ_f [-]	$Q_{f,o}$ [m^3/s]	q [-]	V_p [m^3]
1.08	1.241×10^{-6}	0.86	4.179×10^{-6}
1.30	1.238×10^{-6}	0.85	4.099×10^{-6}
2.14	1.226×10^{-6}	0.84	4.008×10^{-6}

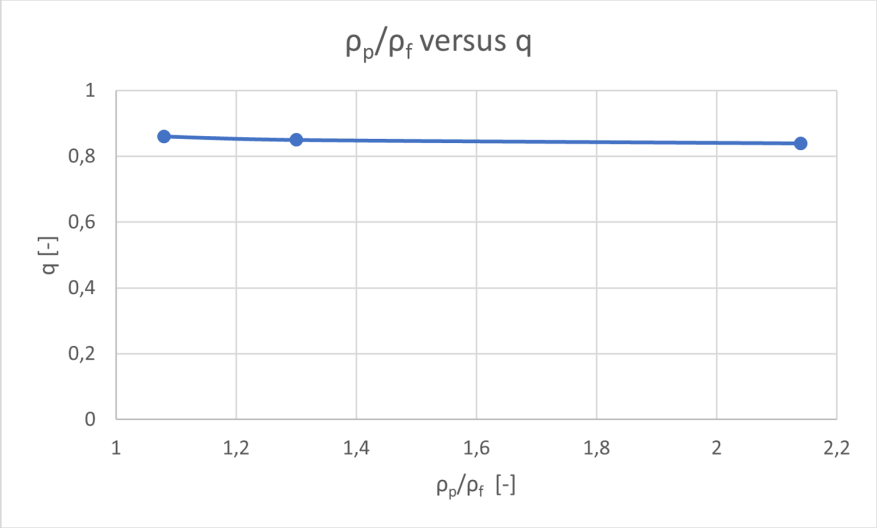

Figure 5.18: Plot of the final normalized fluid flow rate at the outlet q versus particle-fluid density ratio ρ_p/ρ_f.

5.2.3 Combination of particles sizes

This section of the project analyses the efficiency of the LCM in clogging the porous medium by injecting different combinations of solid particles. The cases studied in this work are reported below:

- Case 1: Injecting only particles with diameter of d_p=1.5×10^{-3} m for 0.5 seconds, as a standard case for making comparisons;
- Case 2: Intersperse the injection of one wave (n_{part}=70) of particles with d_p=1.5×10^{-3} m with one wave (n_{part}=70) of particles with d_p=0.5×10^{-3} m for 0.5 seconds;
- Case 3: Intersperse the injection of one wave (n_{part}=70) of particles with d_p=1.5×10^{-3} m with five waves (n_{part}=350) of particles with d_p=0.5×10^{-3} m for 0.5 seconds;
- Case 4: Injecting only particles with diameter of d_p=1.5×10^{-3} m for 0.5 seconds, and then injecting five times the amount of particles with diameter of d_p=0.5×10^{-3} m for 0.5 seconds;
- Case 5: Intersperse the injection of one wave (n_{part}=70) of particles with d_p=1.5×10^{-3} m with one wave (n_{part}=70) of particles with d_p=1.0×10^{-3} m for 0.5 seconds.

Figure 5.20 monitors the particle flow rate $\dot{n}_{part}$ [n_{part}/s] for the analysis of different particles injection combinations. For case 2, because IT is injected twice the amount of particles in the domain in comparison with case 1, it gets twice as much $\dot{n}_{part}$. Because there are more particles in the system, is visible a decreasing trend in $\dot{n}_{part}$, indicating that particles are leaving through the inlet before the end of the injection. For case 3, it is injected five times the amount of particles with

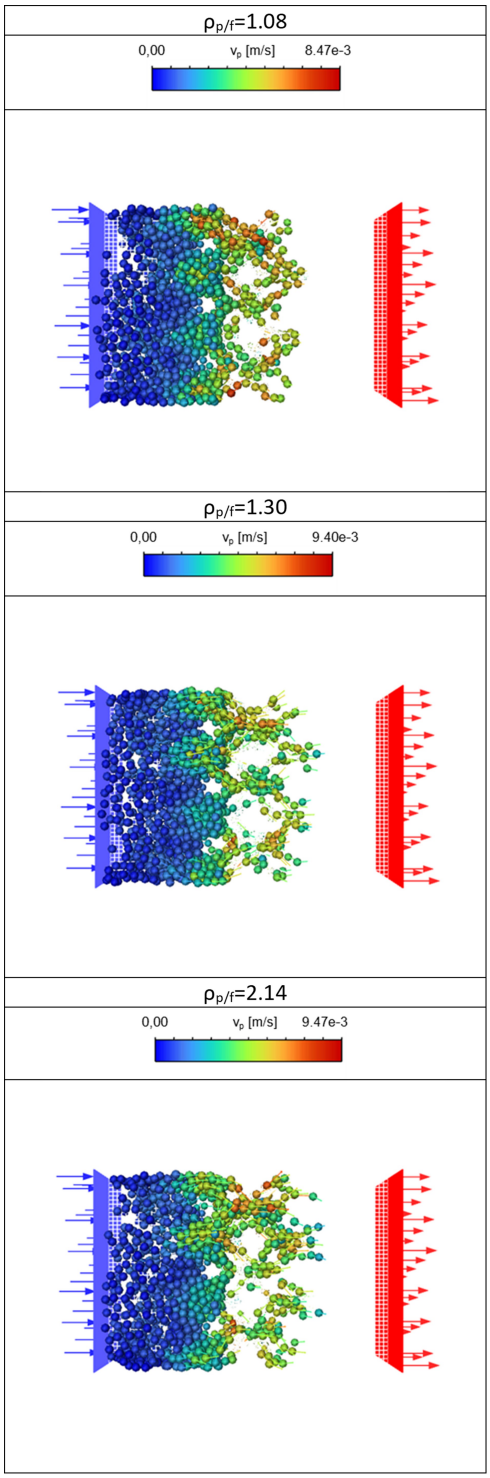

Figure 5.19: Filter formation at t=5s, analysing the particle-fluid density ratio $\rho_{p/f}$ variation.

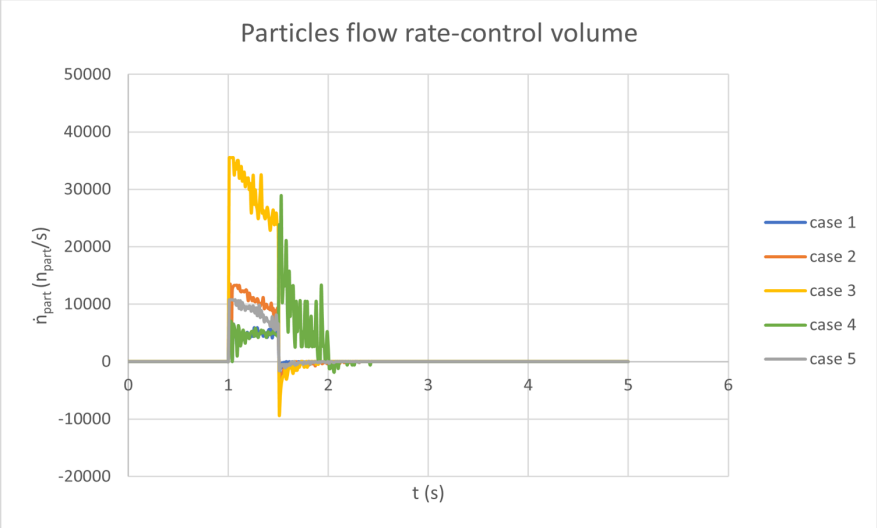

Figure 5.20: Plot of the solid particle flow rate $\dot{n}_{part}$ versus time t, analysing different particles injection combinations.

d_p=0.5×10^{-3} m, so the $\dot{n}_{part}$ increases considerably. Because of the high amount of particles injected, some particles collide with each other or the walls and end up leaving the system through the inlet surface. In case 4, for the period of time of t=1.0-1.5 s, the n_{part} shows the same behavior as case 1. But during t=1.5-2.0 s, there is a considerable increase of particles in the system, in agreement with the fact that five times more particles are injected in this time period. In case 4 it is also visible a decreasing trend in $\dot{n}_{part}$, due to the fact that a particle filter is already formed with d_p=1.5×10^{-3} m, not leaving much space for all d_p=0.5×10^{-3} m to be allocated in the system. In case 5, it has particles with a larger diameter, which form a particle filter faster. This leads to particles colliding with each other and changing directions to escape through the inlet surface.

Figure 5.21 plots the fluid velocity at the outlet surface $v_{f,o}$ [m/s] for the different particles injection combinations. In the time period of t=1.0-1.5s it is possible to see an increase in $v_{f,o}$ for cases 2, 3, and 5, in comparison with case 1. This phenomenon happens due to the fact that in those cases we have a higher particle mass flow $\dot{m}_p$. Even if case 3 has five times more particles with d_p=0.5×10^{-3} m, it does not affect considerably the $v_{f,o}$ curve. Case 4 has the same behavior as case 1 for t=1.0-1.5s, but in period t=1.5-2.0s, $v_{f,o}$ is above the other cases, as in this case the injection of particles is done in two different time periods. After 2 seconds of simulation, cases 2 and 4 have similar behavior to case 1, indicating a low influence of the particles of size d_p=0.5×10^{-3} m. Although, in case 3, interspersing a high quantity of d_p=0.5×10^{-3} m particles with d_p=1.0×10^{-3} m has a larger influence on the fluid flow. In case 5, the curve behavior is similar to case 3, as larger particles are more likely to be captured by the porous medium.

Figure 5.22 monitors the normalized fluid flow rate at the outlet surface, q [-],

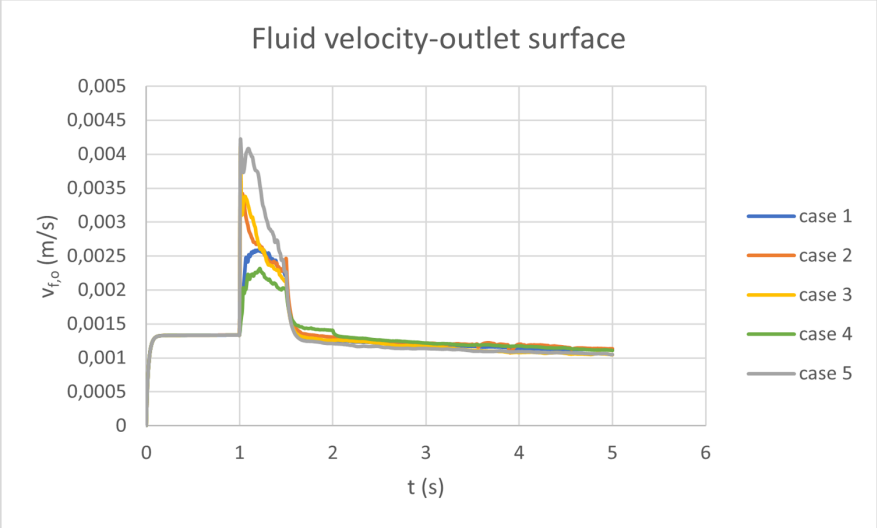

Figure 5.21: Plot of the fluid velocity at the outlet surface $v_{f,o}$ versus time t, analysing different particles injection combinations.

for the different particle injection combinations. During the time period t=1.0-1.5s, it is possible to see an increase in q for cases 2, 3, and 5 when compared with case 1, indicating that a higher particle mass flow $\dot{m}_p$ in the system requires a higher fluid flow to carry the particles. In period t=1.5-2.0 s, case 4 has a higher q than the other cases, because the injection of particles is done in two different periods. The small increase in q indicate that particles with d_p=0.5×10^{-3} m does not require a great increase in q when injected alone. After the injection of solid particles, a steady decrease in q is visible for all cases. Case 2 shows the final results for the reduction of q are very similar to case 1. Case 3 may have a higher increase in q during the injection of particles but is more effective in reducing q. Case 4 presents a better efficiency than case 1, but not as efficient as case 3. Case 5 has high efficiency, similar to case 3, but has a high increase in q during the injection phase.

The total volume occupied by the particles V_p in the domain after 5 seconds of simulation for the analyses of different particles injection combinations are presented in Table 5.8. In case 2, the addition of d_p=0.5×10^{-3} m particles help more d_p=1.5×10^{-3} m particles to remain in the system. In case 3 we observe an increase of d_p=0.5×10^{-3} m in the system, but not compatible with the increase in particles injected. This suggests that the particles are too small, therefore escape more easily. In case 4, more d_p=0.5×10^{-3} m are present in the system, suggesting that the particle filter of d_p=1.5×10^{-3} m particles help the d_p=0.5×10^{-3} m particles to be kept in the system. In case 5, because it used larger particles, the particle filter is formed early, blocking the way for new particles to enter the numerical system. During the drilling of an oil well it is recommended to stop the injection of particles as soon as the filter layer is formed, since the adding of more

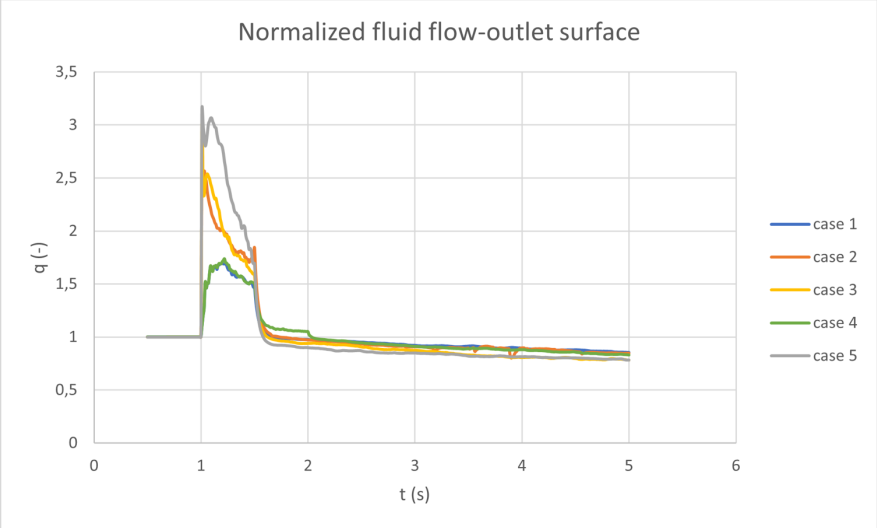

Figure 5.22: Plot of the normalized fluid flow rate at the outlet surface q versus time t, analysing different particles injection combinations.

Table 5.6: Results for V_p [m^3], $Q_{f,o}$ [m^3/s] and q [-] after 5 seconds of simulation for the variation of different particles injection combinations.

Case	$Q_{f,o}$ [m^3/s]	q [-]	V_p [m^3]
1	1.238×10^{-6}	0.85	4.099×10^{-6}
2	1.229×10^{-6}	0.84	4.713×10^{-6}
3	1.138×10^{-6}	0.78	5.022×10^{-6}
4	1.135×10^{-6}	0.82	4.179×10^{-6}
5	1.202×10^{-6}	0.78	5.349×10^{-6}

particles with not contribute to the filter formation but will still require the increase in q to carry the particles. The final results for $Q_{f,o}$ is be seen in Table 5.6. Considering $Q_{f,o}$(t=1)=1.450×10^{-6} m^3/s, the final value for q can be calculated. In Figure 5.23 is shown that cases 3 and 5 presents the best efficiency.

Figure 5.24 visualize the filter at the end of the simulation t=5 s, for every variation in particle injection combinations. In cases 2, 3, and 5, the two types of particles are mixed in the particle filter. In those cases, the smaller particles try to fill the voids created by using only d_p=1.5×10^{-3} m particles. In case 4, the particle filter can be divided into two layers. First, the d_p=1.5×10^{-3} m particles fill the porous medium and create an external filter, and then , d_p=0.5×10^{-3} m particles are deposited on top of the existing filter.

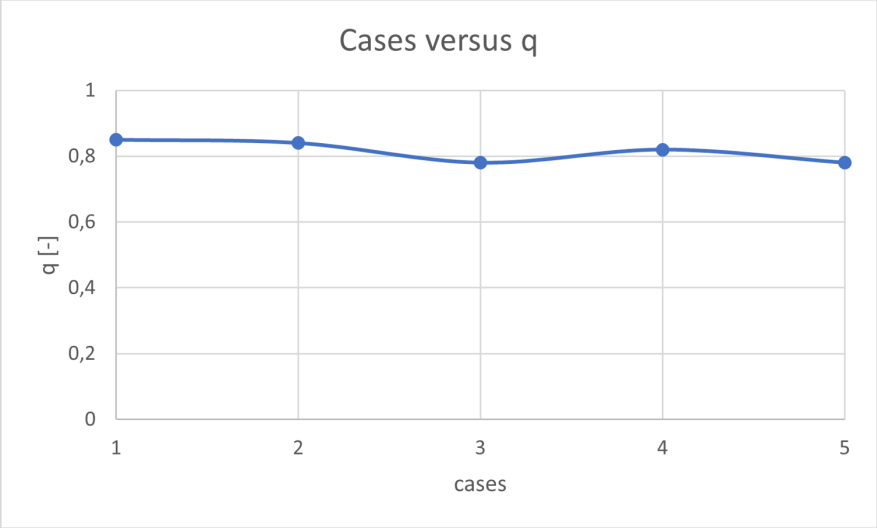

Figure 5.23: Plot of the final normalized fluid flow rate at the outlet q versus multiple particle sizes cases.

Table 5.7: Numerical parameters for the solid particles.

ΔP [Pa]	Δt_f [s]	v_{inj} [m/s]
10	2×10^{-2}	0.2
25	8×10^{-3}	0.4
50	4×10^{-3}	0.55
75	2.5×10^{-3}	0.81
100	2×10^{-3}	1.1

5.3 Pressure difference

This section of the project evaluates the effects of the variation in the pressure difference ΔP over the simulation model during the process of clogging a porous medium. For the analysis of the pressure difference, the following cases are simulated ΔP=(10; 25; 50; 75; 100 Pa). First, a single-phase fluid flow is simulated until the flow reaches a steady state. When the fluid reaches the steady state, the injection of the solid particles occurs with an initial velocity v_{inj} similar to the fluid velocity v_f in each case, as seen in Table 5.7.

Figure 5.25 monitors the particle flow rate $\dot{n}_{part}$ [n_{part}/s]. Due to the increase in ΔP, the solid particles have a higher tendency to be dragged by the flow, resulting in fewer particles leaving the simulation model through the inlet surface during the injection phase. On the other hand, the cases with high pressures tend to force the particles through the entire porous medium and leave them on the outlet surface. This can be seen in the presence of interference in the curves in Figure 5.25 after the injection of particles.

Figure 5.26 monitors the fluid velocity at the outlet surface $v_{f,o}$ [m/s]. Lar-

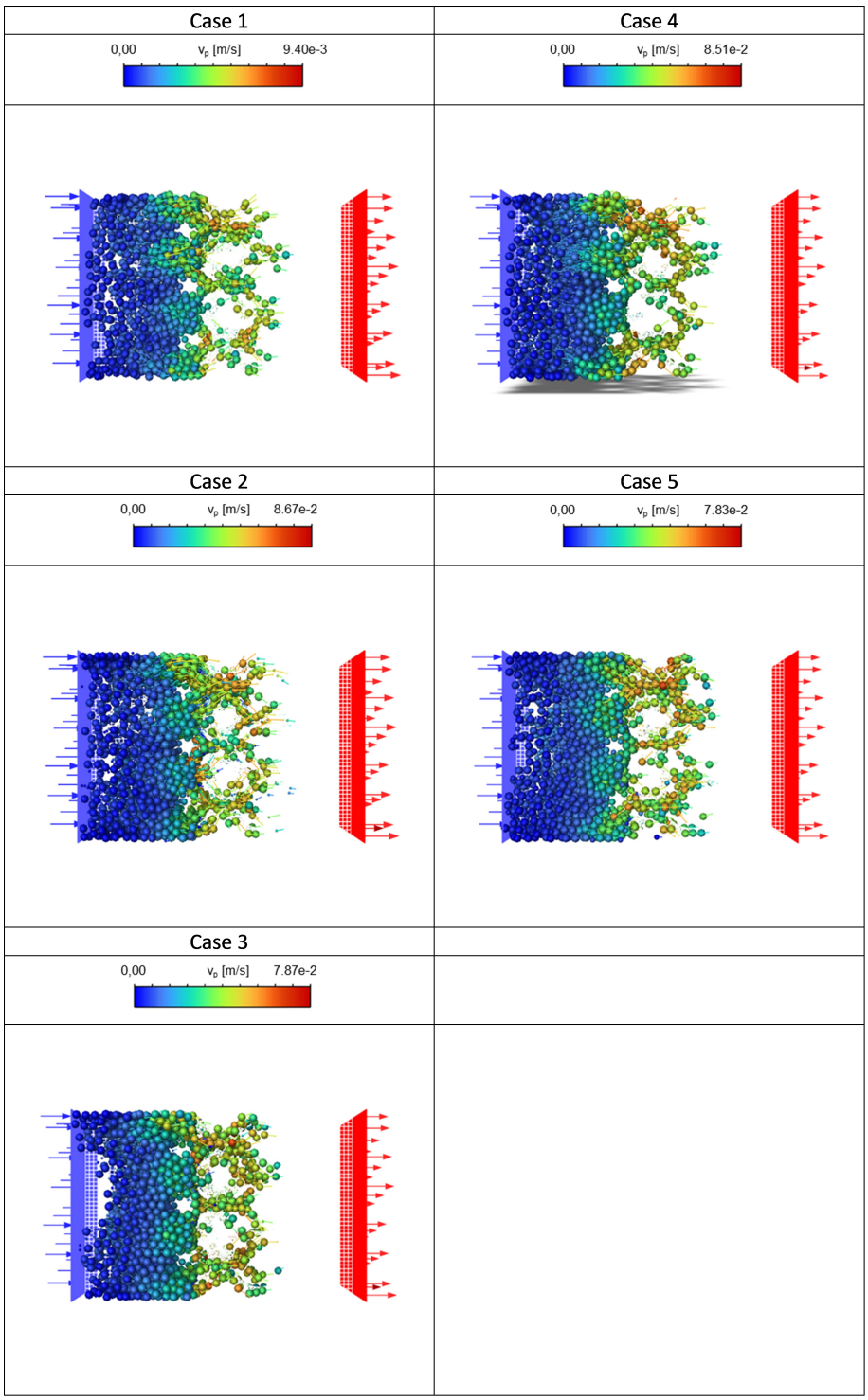

Figure 5.24: Filter formation at t=5s, analysing different particles injection combinations.

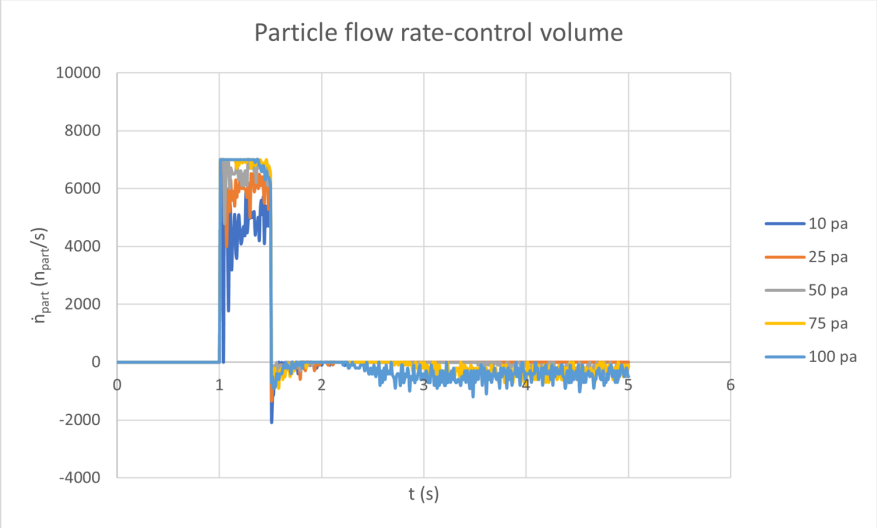

Figure 5.25: Plot of the solid particles flow rate $\dot{n}_{part}$ versus time t, analysing pressure difference ΔP.

ger ΔP requests higher $v_{f,o}$ in the initial stage before the injection. During the injection of solid particles, the mixture of fluid and solids becomes heavier and demands an increase in $v_{f,o}$ to enable the fluid to carry the particles. It is perceptible that $v_{f,o}$ decreases to a lower level than when it was in a steady state, which suggests a successful formation of a particle filter outside the porous medium.

Figure 5.27 monitors the normalized fluid flow rate at the outlet surface q [-]. Similar to the $v_{f,o}$ plot, it is possible to see an increase in q during the injection of particles. In the next stage, q starts reducing when the particles start clogging the porous medium. Finally, q reaches a new steady-state with a value smaller than the initial one, indicating the effectiveness of the particle filter in combating the loss of circulation. It is also noticeable that in all cases the final result converges to approximately the same q but at a different time. The case for 10 Pa does not appear to be as effective as the other cases, but it still has a decreasing tendency. This case may reach the same level as the others if the simulation is continued for longer.

The volume occupied by the particles V_p in the domain after 5 seconds of simulation is presented in Table 5.8. It is visible that the final V_p increases when ΔP increases until 50 Pa. Because higher pressures force the solid particles to follow the fluid flow, avoiding it to escape through the inlet surface. Nonetheless, when $\Delta P \geq$75 Pa, the final V_p reduces, because higher pressures force the particles to go through the whole domain and exit through the outlet surface. Because ΔP influences the $Q_{f,o}$ of the fluid flow, both the initial and final $Q_{f,o}$ of the simulations is presented in Table 5.8, together with the final value for q. In Figure 5.28 is shown that for ΔP 10 Pa q is around 0.85 and drops to 0.75 when $\Delta P \leq$25 Pa.

Figure 5.29 presents the filter formation at the end of the simulation at t=5s

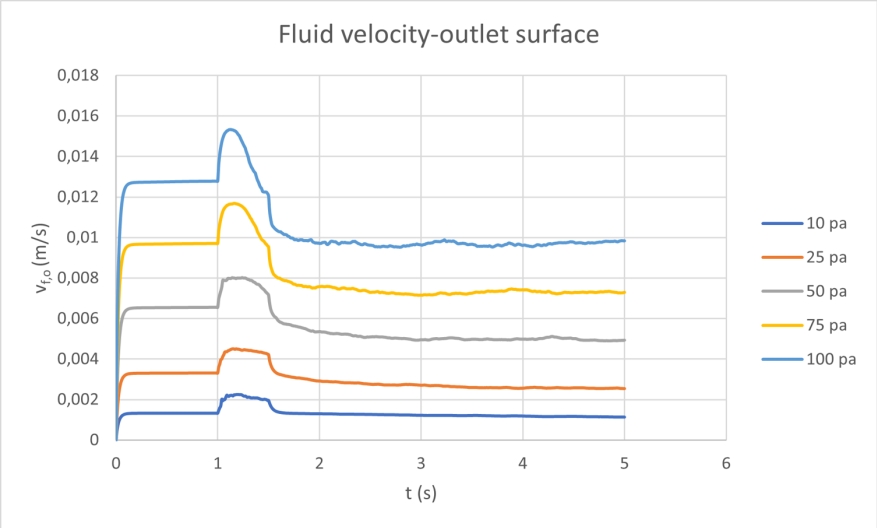

Figure 5.26: Plot of the fluid velocity at the outlet surface $v_{f,o}$ versus time t, analysing pressure difference ΔP.

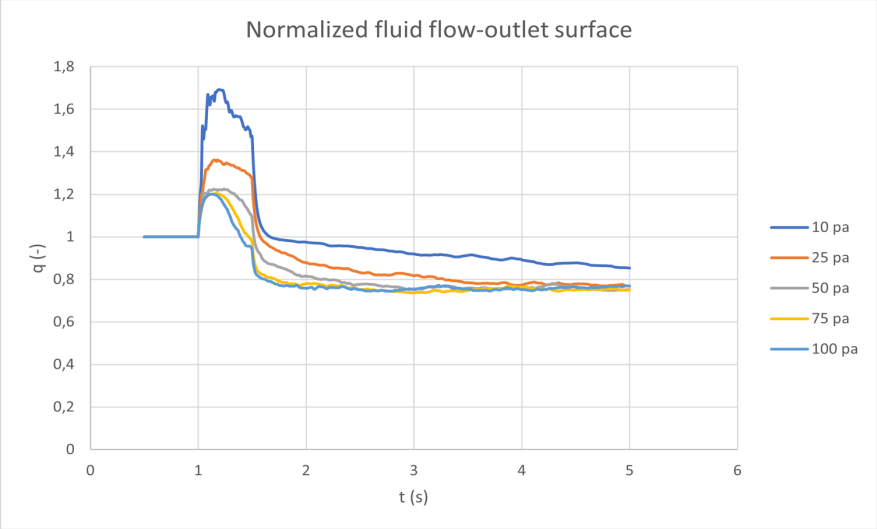

Figure 5.27: Plot of the normalized fluid flow rate at the outlet surface q versus time t, analysing pressure difference ΔP.

Table 5.8: Results for V_p [m^3], $Q_{f,o}$ [m^3/s] and q [-] after 5 seconds of simulation for the variation of pressure difference ΔP [Pa].

ΔP [Pa]	$Q_{f,o}$ (initial) [m^3/s]	$Q_{f,o}$ (final) [m^3/s]	q [-]	V_p [m^3]
10	1.450×10^{-6}	1.238×10^{-6}	0.85	4.099×10^{-6}
25	3.600×10^{-6}	2.762×10^{-6}	0.76	5.135×10^{-6}
50	7.112×10^{-6}	5.349×10^{-6}	0.75	5.280×10^{-6}
75	1.053×10^{-5}	7.913×10^{-6}	0.74	4.796×10^{-6}
100	1.386×10^{-5}	1.067×10^{-5}	0.76	3.841×10^{-6}

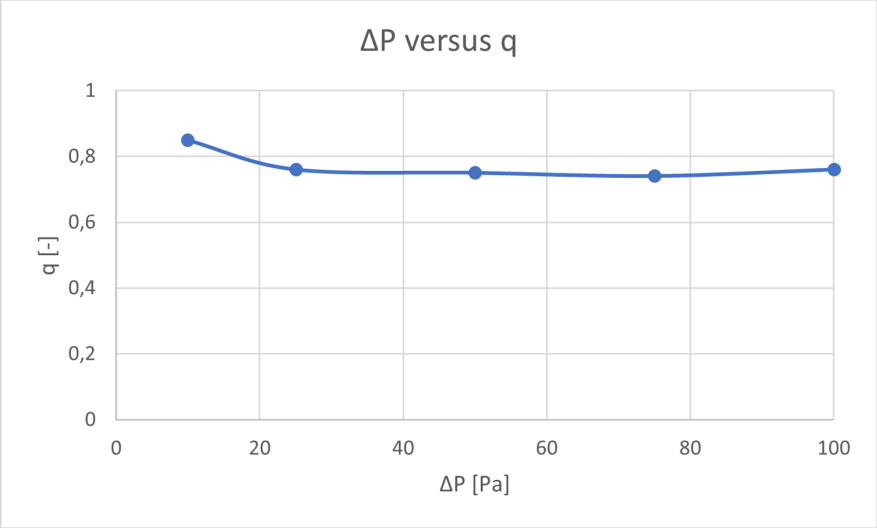

Figure 5.28: Plot of the final normalized fluid flow rate at the outlet q versus pressure difference ΔP.

for every ΔP. The increase in ΔP results in the filter formation outside the porous medium getting more compact. Another aspect to note is that the higher the ΔP, the more particles are dragged through the porous medium and exit on the outlet surface. The increase in ΔP generates a increase in fluid velocity $v_{f,0}$, leading to a increase in particle velocity v_p. It is possible to see that the increase of v_p is proportional to the increase in ΔP in Figure 5.29.

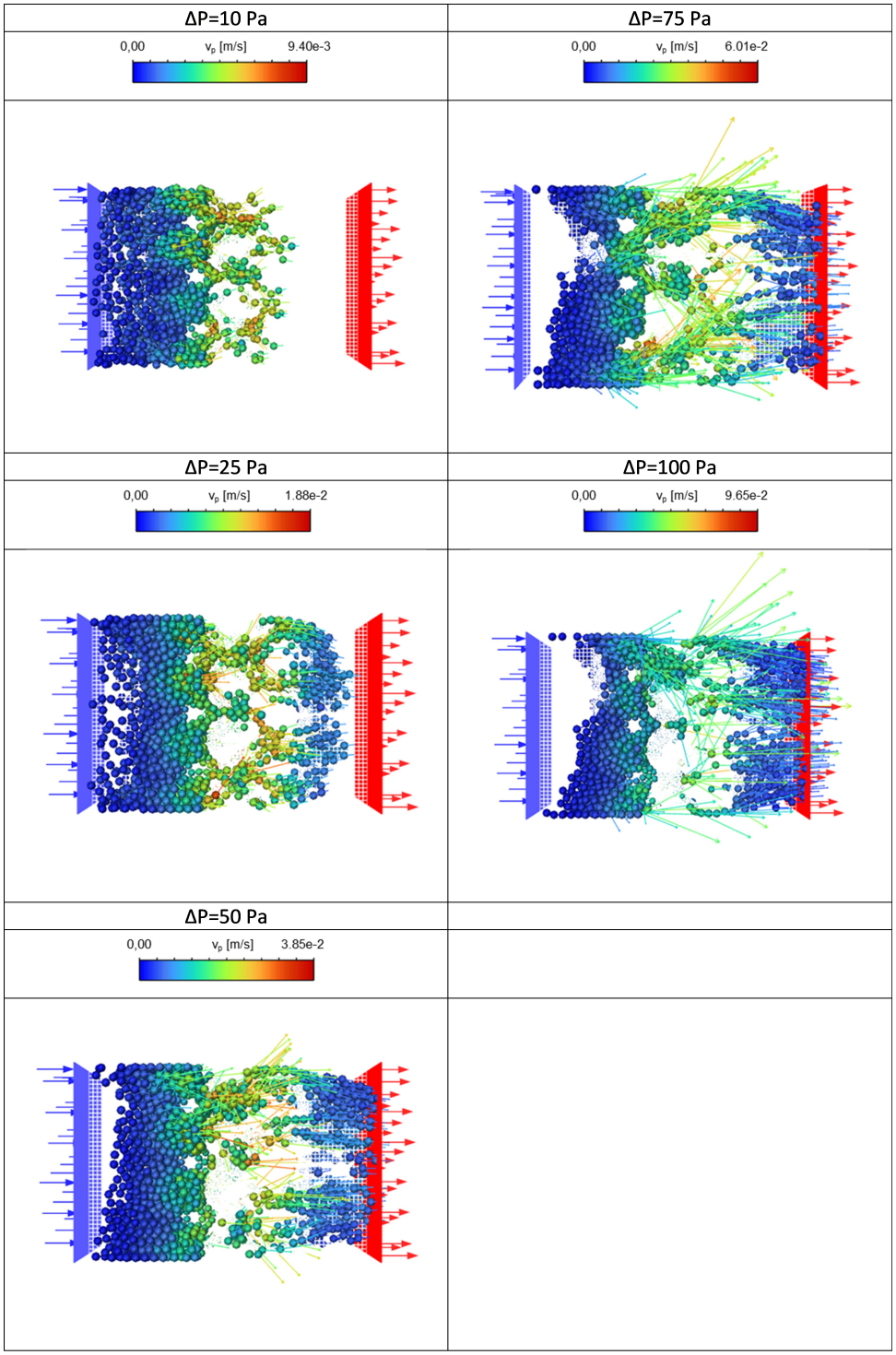

Figure 5.29: Filter formation at t=5s, analysing the pressure difference ΔP variation.

Chapter 6

Conclusion

In the present work, we used a numerical approach to investigate the effectiveness of solid particles to combat the phenomena of lost circulation in rock formations. The rock formation is modeled as a horizontal square channel with a pack of spheres representing a porous medium.

The flow of particles through the porous medium is evaluated in an Euler-Lagrange perspective, where it can be visually separated from the discreet phase from the continuous phase. The liquid-solid flow is solved using the DDPM, while the DEM calculates the forces and torques due to particle collisions.

We evaluated the effectiveness of the mud cake formation through the solid particle flow rate, fluid velocity on the outlet surface, the fluid volumetric flow rate at the outlet, and fluid percentage flow rate at the outlet. In the present work, we vary particle diameter, particle-fluid density ratio, multiple particle combination, and pressure difference at the inlet surface. The key findings can be summarized as follows:

- Particles with a small diameter d_p are not capable of reducing the permeability of a porous medium, and if a particle has a large diameter, it can cause fluid reflux at the inlet surface. For the p_d evaluated in this work, the one with d_p=1.5 mm presented the best results, since it reduced q significantly and did not cause larges turbulence. The case with d_p=2.0 mm is the least recommended one since it can lead to damages in the rock formation.
- For the cases evaluating ρ_p/ρ_f, the final number of particles in the domain is fairly similar. It was concluded that changing ρ_p/ρ_f has small influence on q and the filter formed.
- When analyzing combinations of multiple particles to reduce q, cases 3 and 5 are the most effective. Although both cases present similar final results, case 5 presents a higher fluid loss during the particle injection phase. Therefore, case 3 is the most recommended solution.
- The increase in pressure difference ΔP forces the particles to follow the fluid flow, avoiding the escape of particles at the inlet surface. However, when $\Delta P \geq$50 Pa, the fluid flow is so strong that it forces the solid particles to pass through the porous medium and exit on the outlet surface.

For future works is suggested to analyze other variables, such as the representation of the porous medium structure, and fluid parameters (viscosity and specific mass). Extending the length of the domain is also suggested, to avoid the escape of the solid particles through the inlet surface.

Bibliography

[1] L. Svarovsky, 'Introduction to solid-liquid separation,' in *Solid-Liquid Separation*, Elsevier, 2001, pp. 1–29.

[2] S. A. Bradford and S. Torkzaban, 'Colloid transport and retention in unsaturated porous media: A review of interface-, collector-, and pore-scale processes and models,' *Vadose Zone Journal*, vol. 7, no. 2, pp. 667–681, 2008.

[3] S. L. Sanderson, A. Y. Cheer, J. S. Goodrich, J. D. Graziano and W. T. Callan, 'Crossflow filtration in suspension-feeding fishes,' *Nature*, vol. 412, no. 6845, pp. 439–441, 2001.

[4] E. Papamichos, I. Vardoulakis, J. Tronvoll and A. Skjaerstein, 'Volumetric sand production model and experiment,' *International journal for numerical and analytical methods in geomechanics*, vol. 25, no. 8, pp. 789–808, 2001.

[5] J. Jung, J. Jang, J. C. Santamarina, C. Tsouris, T. Phelps and C. Rawn, 'Gas production from hydrate-bearing sediments: The role of fine particles,' *Energy & fuels*, vol. 26, no. 1, pp. 480–487, 2012.

[6] J. Hwang and M. M. Sharma, 'Filtration in frac packs and its impact on injector performance,' *SPE Production & Operations*, vol. 29, no. 03, pp. 204–215, 2014.

[7] G. C. Howard and P. Scott, 'An analysis and the control of lost circulation,' *Journal of Petroleum Technology*, vol. 3, no. 06, pp. 171–182, 1951.

[8] N. Krygier, A. Solarin and I. Orozova-Bekkevold, 'A drilling company's perspective on non-productive time npt due to well stability issues,' in *SPE Norway Subsurface Conference*, OnePetro, 2020.

[9] J. Cook, F. Growcock, Q. Guo, M. Hodder and E. van Oort, 'Stabilizing the wellbore to prevent lost circulation,' *Oilfield Review*, vol. 23, no. 4, pp. 26–35, 2011.

[10] B. Aadnoy and R. Looyeh, *Petroleum rock mechanics: drilling operations and well design*. Gulf Professional Publishing, 2019.

[11] C. Ezeakacha, S. Salehi, A. Ghalambor and H. Bi, 'Investigating impact of rock type and lithology on mud invasion and formation damage,' in *SPE International Conference and Exhibition on Formation Damage Control*, OnePetro, 2018.

[12] A. S. S. Committee *et al.*, *Drilling fluids processing handbook*. Elsevier, 2011.

[13] R. Caenn, H. C. Darley and G. R. Gray, *Composition and properties of drilling and completion fluids*. Gulf professional publishing, 2011.

[14] D. M. Gala and J. S. Toralde, 'Managed pressure drilling 101: Moving beyond "it's always been done that way,' *The Way Ahead*, vol. 7, no. 01, pp. 12–14, 2011.

[15] A. Lavrov, *Lost circulation: mechanisms and solutions*. Gulf professional publishing, 2016.

[16] D. Elliott, J. Montilva, P. Francis, D. Reitsma, J. Shelton and V. Roes, 'Managed pressure drilling erases the lines,' *Oilfield Review*, vol. 23, no. 1, pp. 14–23, 2011.

[17] S. P. B. Almagro, C. Frates, J. Garand and A. Meyer, 'Sealing fractures: Advances in lost circulation control treatments,' *Oilfield Review*, vol. 26, no. 3, pp. 4–13, 2014.

[18] A. Ghalambor, S. Salehi, M. P. Shahri and M. Karimi, 'Integrated workflow for lost circulation prediction,' in *SPE international symposium and exhibition on formation damage control*, OnePetro, 2014.

[19] D. L. Whitfill and T. Hemphill, 'Pre-treating fluids with lost circulation materials,' *Drilling contractor*, vol. 60, no. 3, pp. 54–57, 2004.

[20] W. F. Rogers, 'Compostion and properties of oil well drilling fluids,' 1948.

[21] A. Rabbani and S. Salehi, 'Dynamic modeling of the formation damage and mud cake deposition using filtration theories coupled with sem image processing,' *Journal of Natural Gas Science and Engineering*, vol. 42, pp. 157–168, 2017.

[22] D. Jiao and M. Sharma, 'Investigation of dynamic mud cake formation: The concept of minimum overbalance pressure,' in *SPE annual technical conference and exhibition*, OnePetro, 1993.

[23] N. Patankar and D. Joseph, 'Lagrangian numerical simulation of particulate flows,' *International Journal of Multiphase Flow*, vol. 27, no. 10, pp. 1685–1706, 2001.

[24] R. H. Davis, E. Herbolzhiemer and A. Acrivos, 'The sedimentation of polydisperse suspensions in vessels having inclined walls,' *International Journal of Multiphase Flow*, vol. 8, no. 6, pp. 571–585, 1982.

[25] G. H. de Lima, F. C. De Lai and S. L. Junqueira, 'Numerical simulation of particulate flow over heterogeneous porous media,' 2017.

[26] M. E. Kokubun, A. Muntean, F. A. Radu, K. Kumar, I. S. Pop, E. Keilegavlen and K. Spildo, 'A pore-scale study of transport of inertial particles by water in porous media,' *Chemical Engineering Science*, vol. 207, pp. 397–409, 2019.

[27] V. G. Poletto, F. C. De Lai and S. L. Junqueira, 'Cfd–dem simulation of mud cake formation in heterogeneous porous medium for lost circulation control,' *Journal of the Brazilian Society of Mechanical Sciences and Engineering*, vol. 42, no. 7, pp. 1–16, 2020.

[28] A. Parvan, S. Jafari, M. Rahnama, A. Raoof *et al.*, 'Insight into particle retention and clogging in porous media; a pore scale study using lattice boltzmann method,' *Advances in Water Resources*, vol. 138, p. 103 530, 2020.

[29] Z. Li, H. Yang, Z. Sun, D. N. Espinoza and M. T. Balhoff, 'A probability-based pore network model of particle jamming in porous media,' *Transport in Porous Media*, pp. 1–27, 2021.

[30] C. G. Thane, 'Geometry and topology of model sediments and their influence on sediment properties,' Ph.D. dissertation, 2006.

[31] P. Bacchin, Q. Derekx, D. Veyret, K. Glucina and P. Moulin, 'Clogging of microporous channels networks: Role of connectivity and tortuosity,' *Microfluidics and nanofluidics*, vol. 17, no. 1, pp. 85–96, 2014.

[32] N.-D. Ahfir, A. Hammadi, A. Alem, H. Wang, G. Le Bras and T. Ouahbi, 'Porous media grain size distribution and hydrodynamic forces effects on transport and deposition of suspended particles,' *Journal of environmental sciences*, vol. 53, pp. 161–172, 2017.

[33] G. Wang, C. Cao, X. Pu and Z. Zhao, 'Experimental investigation on plugging behavior of granular lost circulation materials in fractured thief zone,' *Particulate Science and Technology*, vol. 34, no. 4, pp. 392–396, 2016.

[34] J. Jung, S. C. Cao, Y.-H. Shin, R. I. Al-Raoush, K. Alshibli and J.-W. Choi, 'A microfluidic pore model to study the migration of fine particles in single-phase and multi-phase flows in porous media,' *Microsystem Technologies*, vol. 24, no. 2, pp. 1071–1080, 2018.

[35] J. Zhang, R. She, Z. Dai, R. Ming, G. Ma, X. Cui and L. Li, 'Experimental simulation study on pore clogging mechanism of porous pavement,' *Construction and Building Materials*, vol. 187, pp. 803–818, 2018.

[36] D. A. Nield, A. Bejan *et al.*, *Convection in porous media*. Springer, 2006, vol. 3.

[37] F. Dullien, 'Structure of porous media,' in *Transport Processes in Porous Media*, Springer, 1991, pp. 3–41.

[38] Y. Géraud, F. Mazerolle and S. Raynaud, 'Comparison between connected and overall porosity of thermally stressed granites,' *Journal of Structural Geology*, vol. 14, no. 8-9, pp. 981–990, 1992.

[39] C. Thomas, J. Setién, J. Polanco, J. De Brito and F. Fiol, 'Micro-and macro-porosity of dry-and saturated-state recycled aggregate concrete,' *Journal of Cleaner Production*, vol. 211, pp. 932–940, 2019.

[40] J. Bear, *Dynamics of fluids in porous media*. Courier Corporation, 1988.

[41] P. Cheremskoj, 'Metodi izsleddovania poresti tvurdi tel,' *Moskwa, Energoatomizdat*, 1985.

[42] B. Zdravkov, J. Čermák, M. Šefara and J. Jank, 'Pore classification in the characterization of porous materials: A perspective,' *Open Chemistry*, vol. 5, no. 2, pp. 385–395, 2007.

[43] I. Maryasev, L. Mikhailovskaya, L. Bocharov, E. Chaika, D. Tereshchenko, A. Platonov and G. Platonova, 'Pores: Their classification and role in actual refractory material structures,' *Refractories and Industrial Ceramics*, vol. 52, no. 3, pp. 202–211, 2011.

[44] B. Netinger, 'The effective permeability of a heterogeneous porous medium,' *Transport in porous media*, vol. 15, pp. 99–127, 1994.

[45] M. Chandesris and D. Jamet, 'Jump conditions and surface-excess quantities at a fluid/porous interface: A multi-scale approach,' *Transport in porous media*, vol. 78, no. 3, pp. 419–438, 2009.

[46] R. Dash, K. Mehta and G. Jayaraman, 'Casson fluid flow in a pipe filled with a homogeneous porous medium,' *International Journal of Engineering Science*, vol. 34, no. 10, pp. 1145–1156, 1996.

[47] C. T. Crowe, *Multiphase flow handbook*. CRC press, 2005.

[48] S. M. Peker and S. S. Helvaci, *Solid-liquid two phase flow*. Elsevier, 2011.

[49] E. Loth, 'Particles, drops and bubbles: Fluid dynamics and numerical methods,' *Particles, Drops and Bubbles: Fluid Dynamics and Numerical Methods*, 2010.

[50] G. V. Messa, Q. Yang, O. E. Adedeji, Z. Chára, C. A. R. Duarte, V. Matoušek, M. G. Rasteiro, R. S. Sanders, R. C. Silva and F. J. de Souza, 'Computational fluid dynamics modelling of liquid–solid slurry flows in pipelines: State-of-the-art and future perspectives,' *Processes*, vol. 9, no. 9, p. 1566, 2021.

[51] M. Uhlmann, 'Experience with dns of particulate flow using a variant of the immersed boundary method,' 2006.

[52] M. Chiesa, V. Mathiesen, J. A. Melheim and B. Halvorsen, 'Numerical simulation of particulate flow by the eulerian–lagrangian and the eulerian–eulerian approach with application to a fluidized bed,' *Computers & chemical engineering*, vol. 29, no. 2, pp. 291–304, 2005.

[53] A. B. Yu and B. H. Xu, 'Particle-scale modelling of gas–solid flow in fluidisation,' *Journal of Chemical Technology & Biotechnology: International Research in Process, Environmental & Clean Technology*, vol. 78, no. 2-3, pp. 111–121, 2003.

[54] C. Sun and L. L. Munn, 'Particulate nature of blood determines macroscopic rheology: A 2-d lattice boltzmann analysis,' *Biophysical journal*, vol. 88, no. 3, pp. 1635–1645, 2005.

[55] T. Sparks and G. Chase, 'Air and gas filtration,' *Filters and Filtration Handbook*, p. 117, 2016.

[56] D. C. Mays and J. R. Hunt, 'Hydrodynamic aspects of particle clogging in porous media,' *Environmental science & technology*, vol. 39, no. 2, pp. 577–584, 2005.

[57] A. Santos and P. Bedrikovetsky, 'A stochastic model for particulate suspension flow in porous media,' *Transport in Porous Media*, vol. 62, no. 1, pp. 23–53, 2006.

[58] T. Iwasaki, J. Slade and W. E. Stanley, 'Some notes on sand filtration [with discussion],' *Journal (American Water Works Association)*, vol. 29, no. 10, pp. 1591–1602, 1937.

[59] J. Herzig, D. Leclerc and P. L. Goff, 'Flow of suspensions through porous media—application to deep filtration,' *Industrial & Engineering Chemistry*, vol. 62, no. 5, pp. 8–35, 1970.

[60] P. Shutong and M. M. Sharma, 'A model for predicting injectivity decline in water-injection wells,' *SPE Formation Evaluation*, vol. 12, no. 03, pp. 194–201, 1997.

[61] M. Elimelech, J. Gregory and X. Jia, *Particle deposition and aggregation: measurement, modelling and simulation*. Butterworth-Heinemann, 2013.

[62] F. Civan, 'Temperature effect on power for particle detachment from pore wall described by an arrhenius-type equation,' *Transport in Porous Media*, vol. 67, no. 2, pp. 329–334, 2007.

[63] M. Sharma and Y. Yortsos, 'Transport of particulate suspensions in porous media: Model formulation,' *AIChE Journal*, vol. 33, no. 10, pp. 1636–1643, 1987.

[64] A. Eidsath, R. Carbonell, S. Whitaker and L. Herrmann, 'Dispersion in pulsed systems—iii: Comparison between theory and experiments for packed beds,' *Chemical Engineering Science*, vol. 38, no. 11, pp. 1803–1816, 1983.

[65] O. Coulaud, P. Morel and J. Caltagirone, 'Numerical modelling of nonlinear effects in laminar flow through a porous medium,' *Journal of Fluid Mechanics*, vol. 190, pp. 393–407, 1988.

[66] M. Sahraoui and M. Kaviany, 'Slip and no-slip velocity boundary conditions at interface of porous, plain media,' *International Journal of Heat and Mass Transfer*, vol. 35, no. 4, pp. 927–943, 1992.

[67] S. Lee and J. Yang, 'Modeling of darcy-forchheimer drag for fluid flow across a bank of circular cylinders,' *International journal of heat and mass transfer*, vol. 40, no. 13, pp. 3149–3155, 1997.

[68] R. Larson and J. J. Higdon, 'A periodic grain consolidation model of porous media,' *Physics of Fluids A: Fluid Dynamics*, vol. 1, no. 1, pp. 38–46, 1989.

[69] M. Inoue and A. Nakayama, 'Numerical modeling of non-newtonian fluid flow in a porous medium using a three-dimensional periodic array,' 1998.

[70] G. G. Szpiro, 'Kepler's conjecture,' *Hoboken: Wiley*, 2003.

[71] B. Popoff and M. Braun, 'A lagrangian approach to dense particulate flows,' in *International Conference on Multiphase Flow, Leipzig, Germany*, 2007.

[72] B. P. B. Hoomans, *Granular dynamics of gas-solid two-phase flows*. Universiteit Twente, 2000.

[73] J. Happel and H. Brenner, *Low Reynolds number hydrodynamics: with special applications to particulate media*. Springer Science & Business Media, 2012, vol. 1.

[74] J. E. Matsson, *An Introduction to ANSYS Fluent 2021*. SDC Publications, 2021.

[75] J. Crank and P. Nicolson, 'A practical method for numerical evaluation of solutions of partial differential equations of the heat-conduction type,' in *Mathematical Proceedings of the Cambridge Philosophical Society*, Cambridge University Press, vol. 43, 1947, pp. 50–67.

[76] P. A. Cundall and O. D. Strack, 'A discrete numerical model for granular assemblies,' *geotechnique*, vol. 29, no. 1, pp. 47–65, 1979.

[77] K. J. Dong, R. Zou, R. Yang, A. Yu and G. Roach, 'Dem simulation of cake formation in sedimentation and filtration,' *Minerals Engineering*, vol. 22, no. 11, pp. 921–930, 2009.

[78] H. Kruggel-Emden, E. Simsek, S. Rickelt, S. Wirtz and V. Scherer, 'Review and extension of normal force models for the discrete element method,' *Powder Technology*, vol. 171, no. 3, pp. 157–173, 2007.

[79] A. J. Chorin, 'Numerical solution of the navier-stokes equations,' *Mathematics of computation*, vol. 22, no. 104, pp. 745–762, 1968.

[80] W. K. Anderson and D. L. Bonhaus, 'An implicit upwind algorithm for computing turbulent flows on unstructured grids,' *Computers & Fluids*, vol. 23, no. 1, pp. 1–21, 1994.

[81] S. V. Patankar, *Numerical heat transfer and fluid flow*. CRC press, 2018.

[82] S. Vasquez, 'A phase coupled method for solving multiphase problems on unstructured mesh,' in *ASME 200 Fluids Engineering Division Summer Meeting*, 2000.

[83] S. V. Patankar and D. B. Spalding, 'A calculation procedure for heat, mass and momentum transfer in three-dimensional parabolic flows,' in *Numerical prediction of flow, heat transfer, turbulence and combustion*, Elsevier, 1983, pp. 54–73.

[84] P. Xu and B. Yu, 'Developing a new form of permeability and kozeny–carman constant for homogeneous porous media by means of fractal geometry,' *Advances in water resources*, vol. 31, no. 1, pp. 74–81, 2008.

[85] M. Amanullah, 'Characteristics, behavior and performance of arc plug-a date seed-based sized particulate lcm,' in *SPE Kingdom of Saudi Arabia Annual Technical Symposium and Exhibition*, OnePetro, 2016.

[86] G. de Souza Fritoli, F. C. De Lai and S. L. de Mello Junqueira, 'Effect of lcm and polymeric additives on mudcake and filtrate rheology parameters,' *Journal of Petroleum Science and Engineering*, vol. 205, p. 108 948, 2021.

[87] N.-H. Kim, Y.-P. Lee, S.-Y. Youn and J.-S. Jurng, 'A study on the pressure loss, heat transfer enhancement and fouling control in a vertical particulate flow,' *KSME Journal*, vol. 10, no. 4, pp. 450–457, 1996.

[88] T. B. Anderson and R. Jackson, 'Fluid mechanical description of fluidized beds. equations of motion,' *Industrial & Engineering Chemistry Fundamentals*, vol. 6, no. 4, pp. 527–539, 1967.

[89] F. Odar and W. S. Hamilton, 'Forces on a sphere accelerating in a viscous fluid,' *Journal of fluid mechanics*, vol. 18, no. 2, pp. 302–314, 1964.

[90] P. Saffman, 'The lift on a small sphere in a slow shear flow,' *Journal of fluid mechanics*, vol. 22, no. 2, pp. 385–400, 1965.

[91] B. Oesterlé and T. B. Dinh, 'Experiments on the lift of a spinning sphere in a range of intermediate reynolds numbers,' *Experiments in Fluids*, vol. 25, no. 1, pp. 16–22, 1998.

[92] L. Mazzei and P. Lettieri, 'Cfd simulations of expanding/contracting homogeneous fluidized beds and their transition to bubbling,' *Chemical Engineering Science*, vol. 63, no. 24, pp. 5831–5847, 2008.

[93] S. Morsi and A. Alexander, 'An investigation of particle trajectories in two-phase flow systems,' *Journal of Fluid mechanics*, vol. 55, no. 2, pp. 193–208, 1972.

[94] A. Li and G. Ahmadi, 'Dispersion and deposition of spherical particles from point sources in a turbulent channel flow,' *Aerosol science and technology*, vol. 16, no. 4, pp. 209–226, 1992.

Appendix A

Three dimensional fluid flow

In this appendix is presented the mathematical description of the fluid flow in the three direction of the cartesian system. From Equation (4.1) and Equation (4.2), d/dt is the derivative operator,as given by Equation (A.1), while ∇ is the del operator, given by Equation (A.2).

$$\frac{d}{dt} = \frac{\partial}{\partial t} + u_x \frac{\partial}{\partial x} + u_y \frac{\partial}{\partial y} + u_z \frac{\partial}{\partial z} \tag{A.1}$$

$$\nabla = \frac{\partial()}{\partial x} e_i + \frac{\partial()}{\partial y} e_j + \frac{\partial()}{\partial z} e_k \tag{A.2}$$

Considering a three dimensional cartesian volume of control with gravity in the y axis (-9.81 m^2/s), the equations Equation (4.1) and Equation (4.2) become Equation (A.3), Equation (A.4), Equation (A.5) and Equation (A.6).

$$\frac{\partial u_{f,x}}{\partial x} + \frac{\partial u_{f,y}}{\partial y} + \frac{\partial u_{f,z}}{\partial z} = 0 \tag{A.3}$$

$$\frac{\partial u_{f,x}}{\partial t} + u_{f,x}\frac{\partial u_{f,x}}{\partial x} + u_{f,y}\frac{\partial u_{f,x}}{\partial y} + u_{f,z}\frac{\partial u_{f,x}}{\partial z} = -\frac{1}{\rho_f}\frac{\partial P_{f,x}}{\partial x} + \frac{\mu_f}{\rho_f}\left(\frac{\partial^2 u_{f,x}}{\partial x^2} + \frac{\partial^2 u_{f,x}}{\partial y^2} + \frac{\partial^2 u_{f,x}}{\partial z^2}\right) \tag{A.4}$$

$$\frac{\partial u_{f,y}}{\partial t} + u_{f,x}\frac{\partial u_{f,y}}{\partial x} + u_{f,y}\frac{\partial u_{f,y}}{\partial y} + u_{f,z}\frac{\partial u_{f,y}}{\partial z} = -\frac{1}{\rho_f}\frac{\partial P_{f,x}}{\partial y} + \frac{\mu_f}{\rho_f}\left(\frac{\partial^2 u_{f,y}}{\partial x^2} + \frac{\partial^2 u_{f,y}}{\partial y^2} + \frac{\partial^2 u_{f,y}}{\partial z^2}\right) + g \tag{A.5}$$

$$\frac{\partial u_{f,x}}{\partial t} + u_{f,x}\frac{\partial u_{f,z}}{\partial x} + u_{f,y}\frac{\partial u_{f,z}}{\partial y} + u_{f,z}\frac{\partial u_{f,z}}{\partial z} = \\ -\frac{1}{\rho_f}\frac{\partial P_{f,x}}{\partial z} + \frac{\mu_f}{\rho_f}\left(\frac{\partial^2 u_{f,z}}{\partial x^2} + \frac{\partial^2 u_{f,z}}{\partial y^2} + \frac{\partial^2 u_{f,z}}{\partial z^2}\right) \quad \text{(A.6)}$$

The magnitude of the fluid velocity u_f [m/s] must be written as a function of the decomposed orthogonal components of the Cartesian system $u_{f,x}$, $u_{f,y}$ and $u_{f,z}$ [m/s] along of the unit vectors e_x, e_y and e_z, respectively, as defined in Equation Equation (A.7).

$$u_f = u_{f,x}e_x + u_{f,y}e_y + u_{f,z}e_z \quad \text{(A.7)}$$

Appendix B

Forces acting on particles

In this appendix, the forces acting on the particles resulting from the interaction with the fluid are presented. The surface forces are due to the interaction of the fluid on the surface area of the particles.

The drag force $F_{d,s[j]}$ [N], acting on a particle denoted by index j, exerts a resistance to movement due to relative velocity between fluid and particle. It can be expressed according to Equation (B.1) (Crowe 2005), through a generalization of the expression for the Stokes flow and the correlation for the coefficient of drag C_d [-], which can be numerically expressed in different ways, defined according to the particle flow regime. C_d will be further discussed in section 4.3.1. The specific mass of the fluid is represented by ρ_f [kg/m^3], the cross-sectional area of particle j by $A_{p[j]}$ [m^2], the velocity of the fluid in the current line passing through the centroid of particle j by $\mu_{\beta[j]}$ [m/s], particle velocity by $u_{p[j]}$ [m/s] and surface are of particle j by $A_{p[j]}$ [m^2].

$$F_{d,s[j]} = \frac{1}{2} C_d \rho_\beta A_{p[j]} |u_{\beta[j]} - u_{p[j]}| (u_{\beta[j]} - u_{p[j]}) \tag{B.1}$$

The pressure gradient force, $F_{pg,s[j]}$ [N], is expressed in Equation (B.2) as a function of the advective variation of the fluid momentum (T. B. Anderson and Jackson 1967). It is responsible for promoting the acceleration of the fluid around the particle surface. Assuming that $V_{p[j]}$ is the particle volume [m^3], $m_{p[j]}$ is the particle mass [kg] and $\rho_{p[j]}$ is the particle specific mass [kg/m^3],the fluid pressure is denoted by P_β [Pa].

$$F_{pg,s[j]} = -V_{p[j]} \nabla P_\beta = m_{p[j]} \frac{\rho_\beta}{\rho_{p[j]}} (u_{\beta[j]} \nabla \cdot u_{\beta[j]}) \tag{B.2}$$

The force needed to accelerate the fluid in the neighboring area of the particle is denominated virtual mass force $F_{vm,s[j]}$ [N] (Crowe 2005), it is a way to account for the resistance of the continuous phase (inertia) to the movement calculation of the dispersed phase. Equation (B.3) defines $F_{vm,s[j]}$ as a function of the mass constant virtual C_{vm}, which is an experimental parameter (Odar and Hamilton 1964).

$$F_{vm,s[j]} = C_{vm} m_{p[j]} \frac{\rho_\beta}{\rho_{p[j]}} \frac{D}{Dt}(u_\beta - u_p) \tag{B.3}$$

Saffman's lift force $F_{sl,s[j]}$ (Saffman 1965) comes from the presence of a velocity gradient in the surroundings of the particle which causes a force in the area normal to the particle's movement. The force $F_{sl,s[j]}$ [N] is described in Equation (B.4) as a function of the Saffman's lift coefficient C_{sl} and the angular velocity of the fluid $w_{\beta[j]}$ [1/s], Equation (B.5).

$$F_{sl,s[j]} = m_{p[j]} \frac{\rho_\beta}{\rho_{p[j]}} (w_{\beta[j]} \times (u_{\beta[j]} - u_{p[j]}) C_s l) \tag{B.4}$$

$$w_{\beta[j]} = \nabla \times u_{\beta[j]} \tag{B.5}$$

The Magnus lift force $F_{ml,s[j]}$ [N] is the component of the lift force established from the difference in velocities between opposite sides of the particle, generated by the particle rotational movement (Crowe 2005), Equation (B.6). (Oesterlé and Dinh 1998) modeled the Magnus lift coefficient, Equation (B.6), in function of the rotational Reynolds of the particle in Equation (4.6).

$$F_{ml,s[j]} = m_{p[j]} \frac{\rho_\beta}{\rho_{p[j]}} (w_{p[j]} \times (u_{\beta[j]} - u_{p[j]}) C_{ml[j]}) \tag{B.6}$$

$$C_{ml[j]} = 0.45 + \left(\frac{Re_{w[j]}}{Re_{p[j]}} - 0.45 \right) \exp\left(0.0568 Re_{w[j]}^{0.4} Re_{p[j]}^{0.3} \right) \tag{B.7}$$

$$Re_{w[j]} = \frac{\rho_\beta d_{p[j]}^2}{4\mu_\beta} \left| \frac{1}{2} \nabla u_{\beta[j]} - u_{w[j]} \right| \tag{B.8}$$

Buoyancy force, Equation (B.9), is defined as a force proportional to the weight of the fluid displaced by a particle and acts in the opposite direction of the gravitational acceleration (Mazzei and Lettieri 2008).

$$F_{b,b[j]} = -\rho_\beta V_p g \tag{B.9}$$

The body forces act on the volume of a particle due to the presence of an external force field (e.g. electromagnetic field, gravitational field, molecular Van der Waals force,...). In the present work, it is only considered the gravity force $F_{g,b[j]}$, which is described in Equation (B.10).

$$F_{g,s[j]} = \rho_p V_p g \tag{B.10}$$

Appendix C

DDPM-Drag coefficient and Saffman lift force

In this appendix, it is described in more detail the numerical calculations of some terms on the DDPM method.the terms in question are the drag coefficient C_d and for the Saffman lift force $F_{sl,s[j]}$.

The calculation of the drag coefficient C_d present on the the drag force term $F_{d,s[j]}$ uses the method proposed by Morsi and Alexander (1972), Equation (C.1). The method is a function of the Reynolds number of the particle Re_p [-] presented in Equation (4.24). The values for a_1, a_2 and a_3 are presented in Table C.1.

$$C_d = a_1 + \frac{a_2}{Re_p} + \frac{a_3}{Re_p^2} \tag{C.1}$$

For the Saffman lift force $F_{sl,s[j]}$, the Ansys Fluent software uses a generalization of the Equation (B.4) introduced by A. Li and Ahmadi (1992), Equation (C.2). K is equal to 2.594 and d_{ij} is the deformation tensor Equation (C.3).

Table C.1: Values for a_1, a_2 and a_3 in the correlation for the coefficient of drag C_d [-] proposed by Morsi and Alexander (1972).

Re_p	a_1	a_1	a_1
0<Re_p<0.1	0	18	0
0.1<Re_p<1	3.690	22.73	0.0903
1<Re_p<10	1.222	29.1667	-3.8889
10<Re_p<100	0.6167	46.50	-116.67
100<Re_p<1000	0.3644	98.33	-2778
1000<Re_p<5000	0.357	148.62	-47500
5000<Re_p<10000	0.46	-490.546	5787700
10000>Re_p	0.5191	-1662.5	5416700

$$F_{sl,s[j]} = \frac{2C_{sl}(\rho_f \mu_f)^{1/2} d_{ij}}{\rho_p d_p (d_{lk} d_{kl})^{1/4}} (u_{f,j} - u_{p,j}) \tag{C.2}$$

$$d_{ij} = \frac{1}{2}(u_{i,j} + u_{j,i}) \tag{C.3}$$

Appendix D

DEM- Damping and friction coefficient

In this appendix, it is described in more detail the numerical calculations of some terms on the DDPM method.the terms in question are the damping coefficient $\eta_{n[j]}$ and for the friction coefficient μ_f.

The damping coefficient $\eta_{n[j]}$ can refer to the particle-particle collision (p-p subscript) or particle-wall collision (p-w subscript) Equation (D.1). $\eta_{n[j]}$ is a function of the sum of masses of the two particles $m_{[ij]}$, Equation (D.2); the restitution coefficient e_{p-p} Equation (D.3) and the collision time Δt_{col}, Equation (D.4), which is dependent of $k_{n[j]}$. The subscript AC means after collision, while the subscript BC means before collision. The estimation of the time step of the particle Δt_p is adequate when less than half a time step of the collision Δt_{col}.

$$\eta_{n,p-p} = -2\frac{m_{[ij]} ln(e_{p-p})}{\Delta t_{col}}; = \eta_{n,p-w} = -2\frac{m_{[ij]} ln(e_{p-w})}{\Delta t_{col}} \tag{D.1}$$

$$m_{[ij]} = \frac{m_{[i]} m_{[j]}}{m_{[i]} + m_{[j]}} \tag{D.2}$$

$$e_{n,p-p} = \frac{u_{[i,j]}.n_{[i,j]}}{u_{[i,j]}.n_{[i,j]}} \frac{AC}{BC} \tag{D.3}$$

$$\Delta t_{col} = \sqrt{\frac{m_{[ij]}}{k_{n[j]}}(\pi^2 + ln^2(e_{p-p}))} \tag{D.4}$$

The friction coefficient μ_f can be calculated in three different ways, depending on the friction regime. The static regime happens when $|u_{t[ij]}|$ is smaller than the glide velocity $|u_g|$. The sliding regime is when $|u_{t[ij]}|$ is bigger than $|u_g|$ but smaller than the limit velocity $|u_l|$. The limit regime is when $|u_{t[ij]}|$ is bigger than $|u_l|$. $|s_l|$ determines how fast μ_g tends to μ_l, all cases are presented in Equation (D.5).

$$\mu_f = \begin{cases} \mu_s + (\mu_s - \mu_g)\left(\frac{|u_{t[ij]}|}{|u_g|} - 2\right)\frac{|u_{t[ij]}|}{|u_g|} & \text{if } |u_g| > |u_{t[ij]}| \\ \mu_g & \text{if } |u_g| < |u_{t[ij]}| < |u_l| \\ \mu_g \frac{1+(|u_{t[ij]}|-|u_l|)/s_l}{1+\mu_g/\mu_l(|u_{t[ij]}|-|u_l|)/s_l} & \text{if } |u_{t[ij]}| > |u_l| \end{cases} \tag{D.5}$$

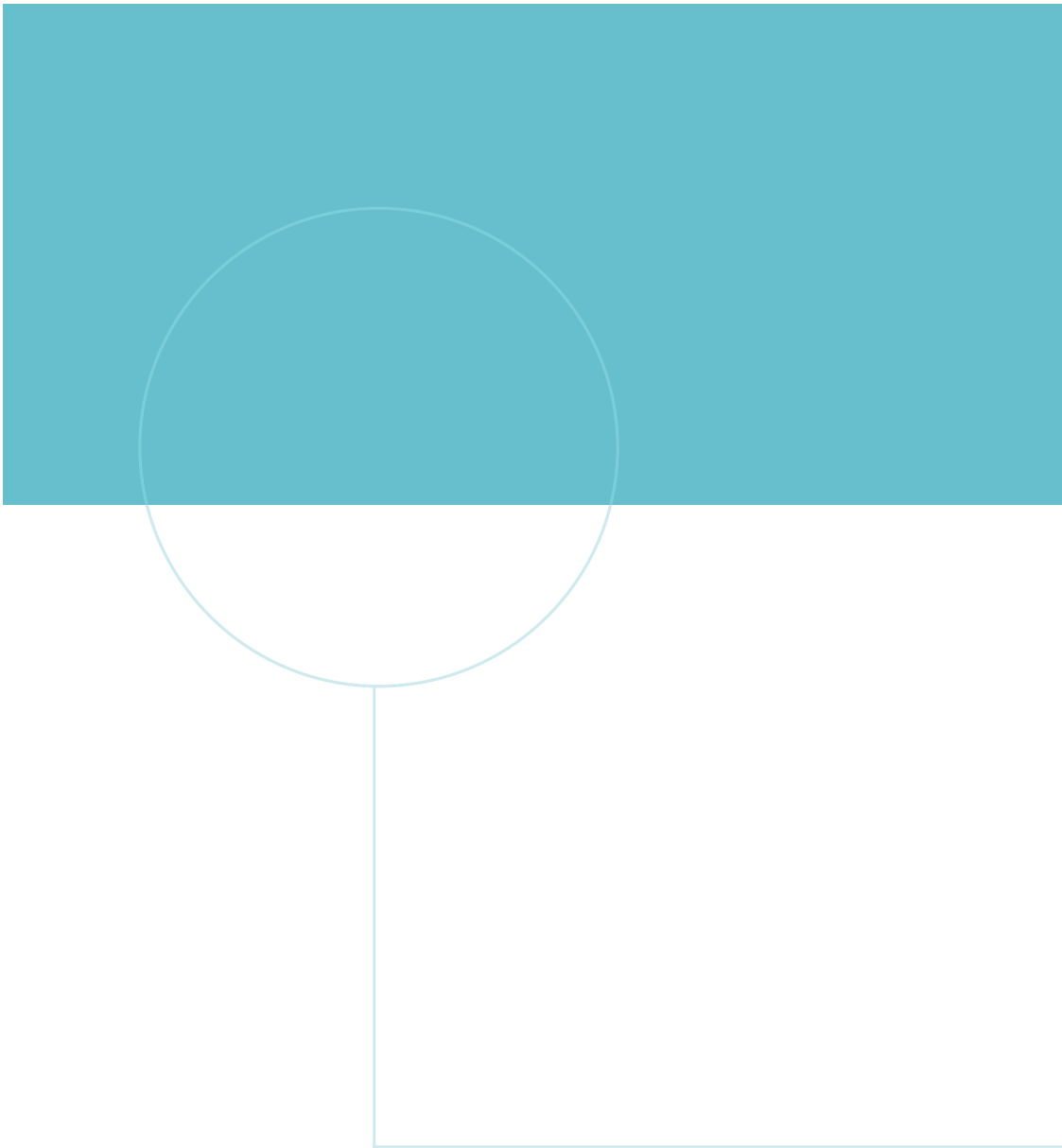

NTNU

Norwegian University of
Science and Technology